XVI. APPLIED PLASMA RESEARCH[*]

A. Active Plasma Systems

Academic Research Staff

Prof. L. D. Smullin
Prof. A. Bers
Prof. R. R. Parker

Graduate Students

N. J. Fisch	G. H. Neilson	A. L. Throop
C. F. F. Karney	M. D. Simonutti	D. C. Watson
J. L. Kulp	M. S. Tekula	P. R. Widing

RESEARCH OBJECTIVES

The research of the Active Plasma Systems group is concerned with the dynamics of highly ionized plasmas and charged-particle beams, with particular emphasis on understanding and exploiting linear and nonlinear interactions in plasmas. In the coming year we shall add a new program of computer symbolic calculations of the nonlinear interaction of waves in a plasma. Some of the major areas of research are listed below.

1. Wave Studies at Lower Hybrid Frequency

We are continuing experimental studies of wave phenomena near lower hybrid frequency. Our present emphasis is on the linear conversion of these modes at the resonant point to warm-plasma ion sound modes that propagate across the magnetic field. The role of nonlinear absorption vs parametric instability is also being investigated. Our goal is to study the feasibility of lower hybrid RF heating of Tokamaks in a small-scale experiment.

R. R. Parker

2. Nonlinear Beam-Plasma Interactions

We have observed a nonlinear interaction between a modulated beam wave and an externally generated plasma wave, which leads to excitation of an ion-acoustic wave. During the coming year we plan to continue investigation of such nonlinear beam-related interactions in order to develop quantitative models of such interactions and determine their role in generating low-frequency spectra in beam-plasma systems.

R. R. Parker

3. Beam-Plasma Source

A new plasma source has been developed which produces dense (10^{12} cm^{-3}), hot (10-20 eV), highly ionized (50%) plasma by extraction from dual beam-plasma sources into a differentially pumped drift region. We plan to make a thorough diagnostic survey

of this plasma, with particular emphasis on the nature and cause of observed low-frequency turbulence. Attempts to stabilize the plasma are also anticipated.

L. D. Smullin, R. R. Parker

4. Computer Analytic Study of Nonlinear Wave Interactions

We are developing and using new computer capabilities in symbolic computation. At present we are applying this procedure to the problem of nonlinear wave interactions in a plasma. The coupling coefficients of all possible wave-wave interactions in a plasma can thus be derived and stored in analytic form by a computer. This will allow us to study the nonlinear parametric interactions of coherent waves, as well as the interaction of many waves for simulation of weak turbulence. This work will be carried out in cooperation with the Project MAC Mathlab, and will use the MACSYMA system.

A. Bers

1. OBSERVATION OF NONLINEAR INTERACTIONS IN
   A BEAM-PLASMA SYSTEM

A. E. Throop, R. R. Parker

Introduction

In this report we shall discuss results of an experimental study of nonlinear wave interactions in a beam-plasma system. Detailed measurements of the waves participating in the interaction have been made, and the results seem consistent with simple three-wave coupling-of-modes theory. Two specific cases will be discussed,[1] both of which use a beam wave to excite lower frequency (LF) plasma modes. In the first case, an unstable ion acoustic spectrum interacts parametrically with a beam wave to excite an idler spectrum at the difference frequency and wave number. In the second case, two high-frequency (HF) waves interact to excite resonantly an acoustic wave. Only the qualitative features of the interactions will be presented here.

Experimental Apparatus

The experimental apparatus is shown schematically in Fig. XVI-1. At one end, a microwave structure produces a plasma column by electron-cyclotron resonance. This plasma is fairly quiescent, with typical density of 5×10^{10} cm^{-3} and electron temperature of 5 eV. At the opposite end of the experiment, an electron beam is injected into the plasma to excite the slow space-charge beam wave (SSCW). The electron source is an oxide-coated cathode that provides a beam with 2-keV energy and 15-mA current. The beam can also be modulated by applying a grid-cathode voltage. The diagnostics are Langmuir and RF probes, which can be scanned both axially and radially. Wire
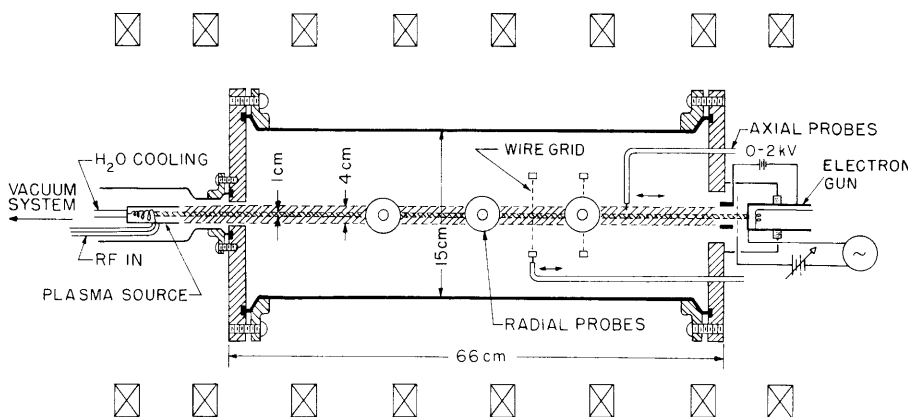
Fig. XVI-1. Experimental apparatus.

grids (6 strands of .003 in. tungsten wire, crossed in wagon-wheel arrangement) are used to launch and detect waves in the plasma. These grids have been found to be useful as a diagnostic for lower frequency waves (~100 kHz). The experiment is operated in a uniform 1-kG magnetic field, and typically uses argon gas at 6×10^{-5} Torr pressure.

Beam Wave Characteristics

Since both interactions use the SSCW as a pump wave, it is important to understand the properties of the beam wave. The basic model[2] in these experiments was the guided-wave dispersion relation (GWDR) shown in Fig. XVI-2. The model assumed a cold plasma and cold beam. The addition of electron thermal effects does not substantially affect the interaction. The GWDR was numerically evaluated for complex $k_{\parallel}$, assuming real ω, and left $k_{\perp}$ as a geometrically determined parameter. Values consistent with our experimental conditions were used to evaluate the dispersion relation. The GWDR predicts that in the presence of the plasma the SSCW will be unstable over a broad frequency band below the electron plasma frequency (f_{pe}).

Figure XVI-3a shows the RF spectrum obtained when the electron beam is injected into the plasma column. As the beam current is increased, the spectrum increases in amplitude and broadens to include lower frequencies. The HF emission can be tuned by varying plasma density (the microwave source power). Langmuir probe measurements also show that the plasma frequency is slightly above the HF emission, as predicted. This confirms that the HF emission is due to the unstable SSCW.

The SSCW used here, however, is obviously not suitable as a pump for narrow-band interactions, because of the lack of coherence and the broadband nature of the spectrum. To obtain a more useful beam wave, we modulate the beam at a frequency within the unstable SSCW region. This entrains the energy into a narrow, well-defined beam wave
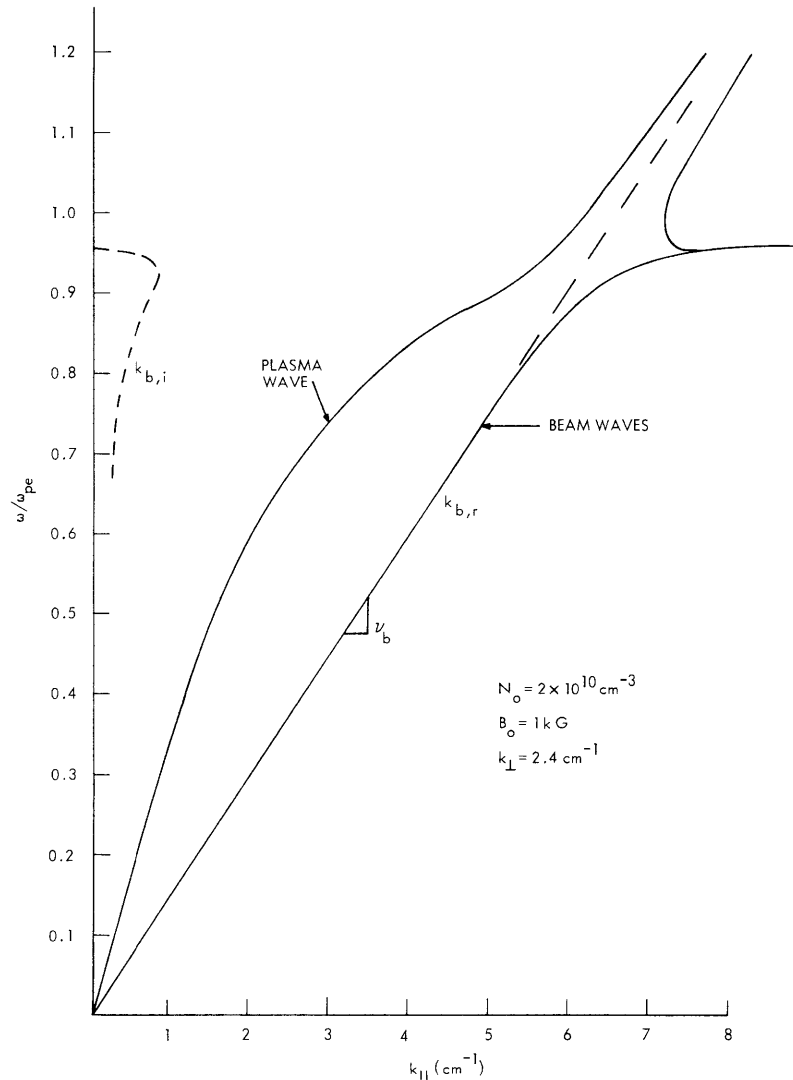
Fig. XVI-2. Guided-wave dispersion relation for cold beam and cold plasma.

at the modulating frequency, as shown in Fig. XVI-3b. Here we display a small portion of the broadband emission of Fig. XVI-3a, but on a greatly expanded frequency scale. The spectrum is centered at the modulating frequency and shows the emission with modulation on and off — all other beam and plasma parameters are unchanged. The bandwidth has been decreased by well over a factor of 1000, while the amplitude change caused by the entrainment is apparent from the photographs.

Figure XVI-4a shows a typical RF interferogram of the entrained beam wave. The wave grows, saturates, and decays over a large axial distance. The saturated region, over which the wave amplitude is quite uniform, is obviously an ideal position in which to study nonlinear interactions. The wavelength of the entrained beam wave can be
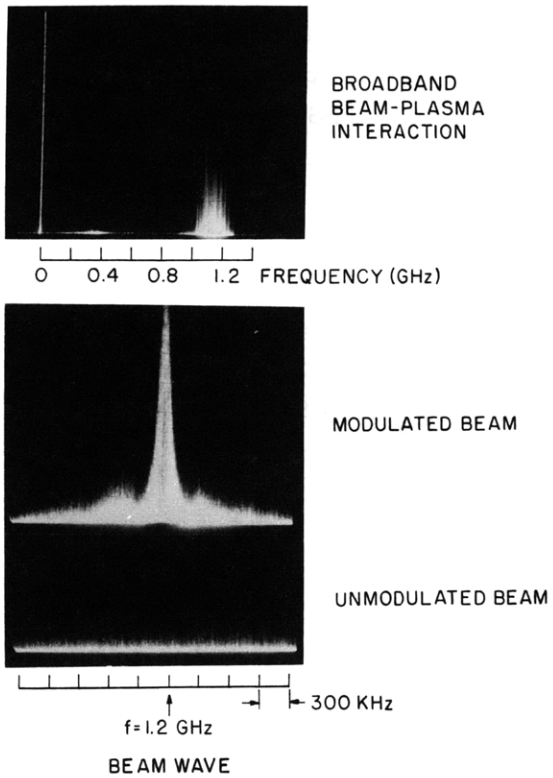
BROADBAND
BEAM-PLASMA
INTERACTION

0   0.4   0.8   1.2   FREQUENCY (GHz)

MODULATED BEAM

UNMODULATED BEAM

⊢ 300 KHz

f = 1.2 GHz

BEAM WAVE

0   5   10   15   20
AXIAL DISTANCE FROM GUN (cm)

(a)

$\omega \sim$ FREQ (×10⁹ Hz)

k_{real}

$v_p = 1.5 \times 10^9$ cm/s

$k \sim \frac{1}{\lambda}$ (cm⁻¹)

(b)

Fig. XVI-3.

(a) RF spectrum of the unmodulated beam injected into plasma.
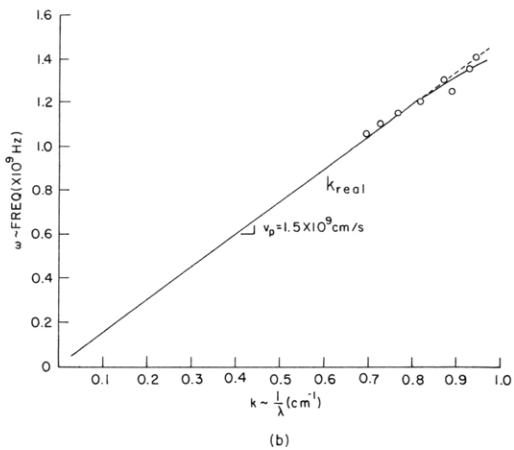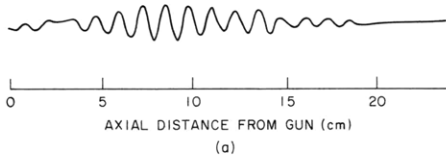(b) Detail of RF spectrum showing energy entrainment. (Same vertical sensitivity in both pictures.)

Fig. XVI-4.

(a) RF interferogram of entrained slow space-charge beam wave (SSCW).
(b) Measured beam wave dispersion relation.

easily measured, and the dispersion relation shown in Fig. XVI-4b is obtained. The beam wave exhibits a phase velocity that corresponds to the gun voltage, and tends to show the expected dispersion as the modulating frequency approaches ω_{pe} (see Fig. XVI-2). These measurements confirm that the modulated SSCW provides a coherent, well-defined wave that can be used as a pump to study nonlinear interactions in the plasma column.

Acoustic Wave Characteristics

Since the expected nonlinear interactions involved coupling to an ion-acoustic wave, the propagation characteristics of these waves were studied in some detail. For these experiments, the waves were launched from the wire grid and an RF probe was used as
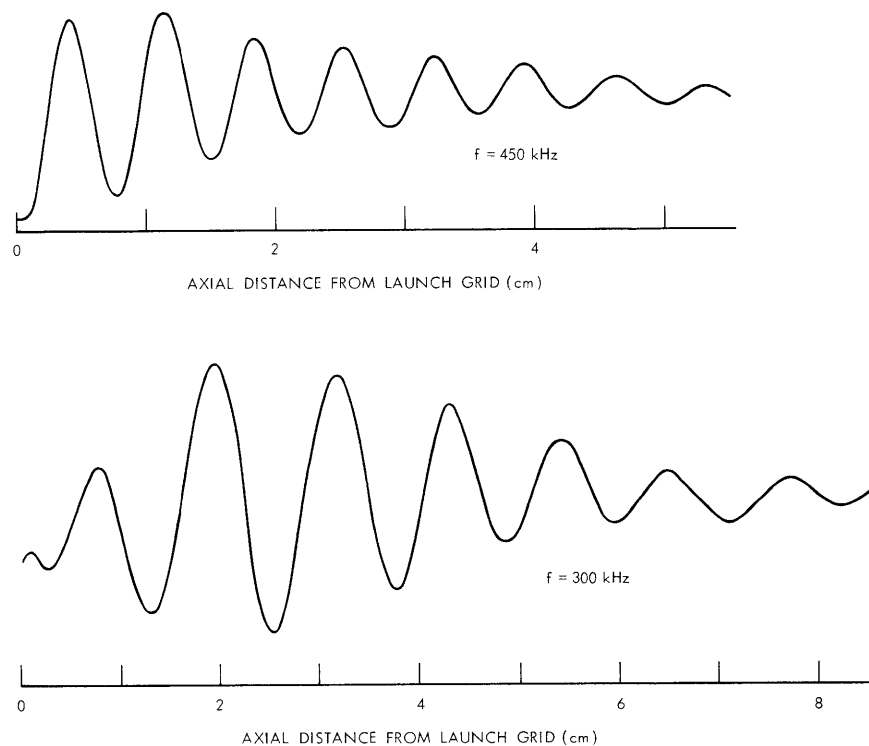

Fig. XVI-5. Examples of interferograms of ion-acoustic waves.

a receiving antenna. Over the 150 kHz-2 MHz frequency range, the wave (in argon) displayed very light damping and, in some cases, even growth in the presence of the beam. Figure XVI-5 shows two examples of typical interferograms. Typical damping rates are in the $(k_i/k_r) \approx 10^{-2}$ range. For frequencies above approximately 2 MHz, however, the waves become highly ion Landau-damped.

Figure XVI-6 shows the acoustic wave dispersion relation measured in the plasma
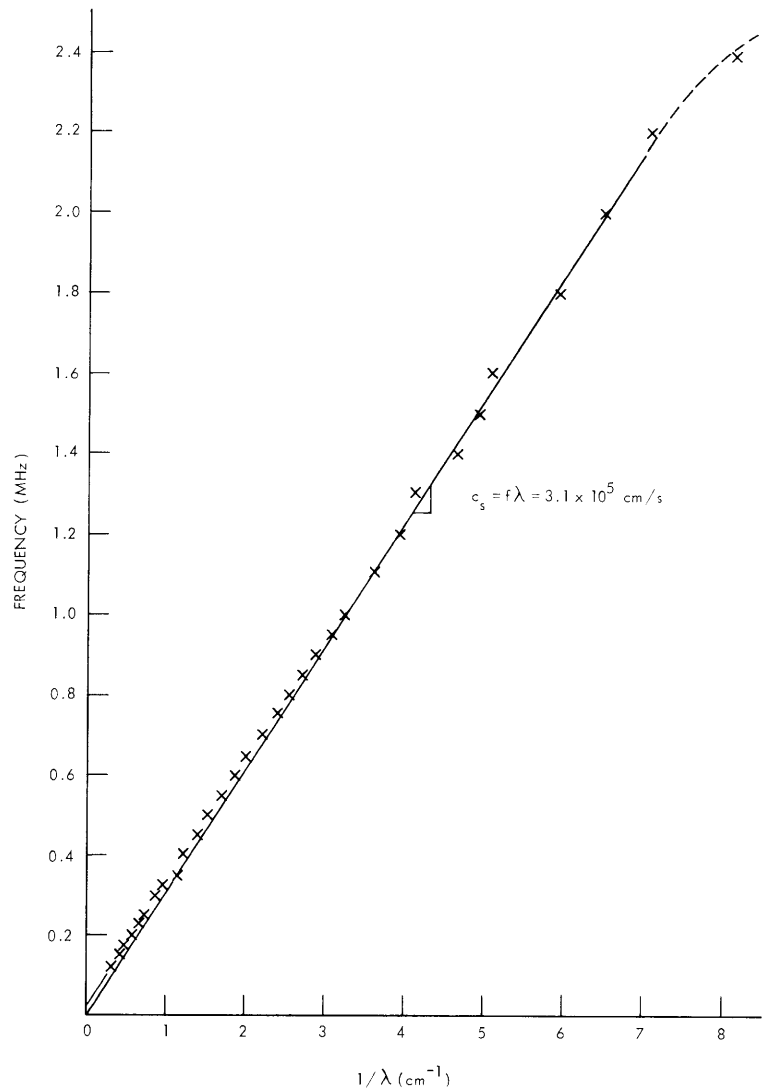
Fig. XVI-6. Measured dispersion relation for ion-acoustic waves.

column without the presence of a beam. The phase velocity of the wave agrees well with the sound speed calculated for argon. The sound speed is not substantially changed by the presence of the beam. The dispersion that occurs at frequencies less than 800 kHz is not fully understood. The GWDR, however, exhibits a similar tendency when it is evaluated in the acoustic regime. In these calculations, the group velocity of the ion-acoustic branch slows considerably near $\omega \approx k_\perp c_s$. This suggests that for small values of $k_\parallel$ a finite $k_\perp$ could contribute to the magnitude of k, and hence cause the observed dispersion.

These data suggest that the lightly damped acoustic spectrum represents a strong fluctuation background. In the presence of free energy, either in the form of the

negative-energy SSCW or parametrically supplied energy, waves can therefore be expected to grow from this fluctuation background.

Parametric Interaction

Under certain beam and plasma conditions, it is possible to excite a low-frequency spectrum such as that shown in Fig. XVI-7a. The spectrum typically extends over the 0.1-2 MHz frequency range, which is the same frequency band over which the acoustic spectrum is lightly damped. This and other data suggest that the spectrum grows from

FREQUENCY (MHz)

(a)
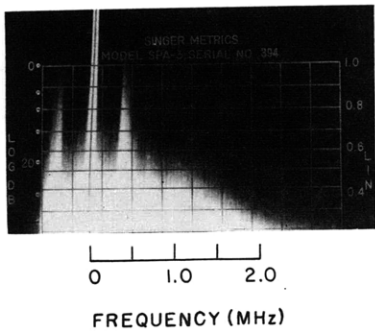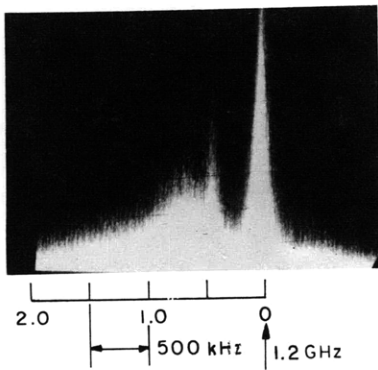
Fig. XVI-7.

(a) Low-frequency spectrum excited by electron beam.
(b) Sideband produced by the IF spectrum parametrically interacting with beam wave.

(b)

an unstable acoustic branch, although the specific details of the generation of this spectrum are not of interest in this report.

If we now introduce an HF pump in the form of an entrained beam wave, the LF spectrum can interact parametrically with it to produce an ω- and k-matching idler wave.[3] This is demonstrated by the HF spectrum shown in Fig. XVI-7b, which was taken simultaneously with Fig. XVI-7a. The idler and LF spectra are mirror images of each other, as expected, and have the same general profile. The slightly smaller spectral width of the idler spectrum is probably caused by threshold effects. This interaction
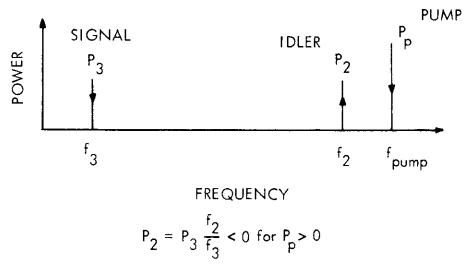
Fig. XVI-8.
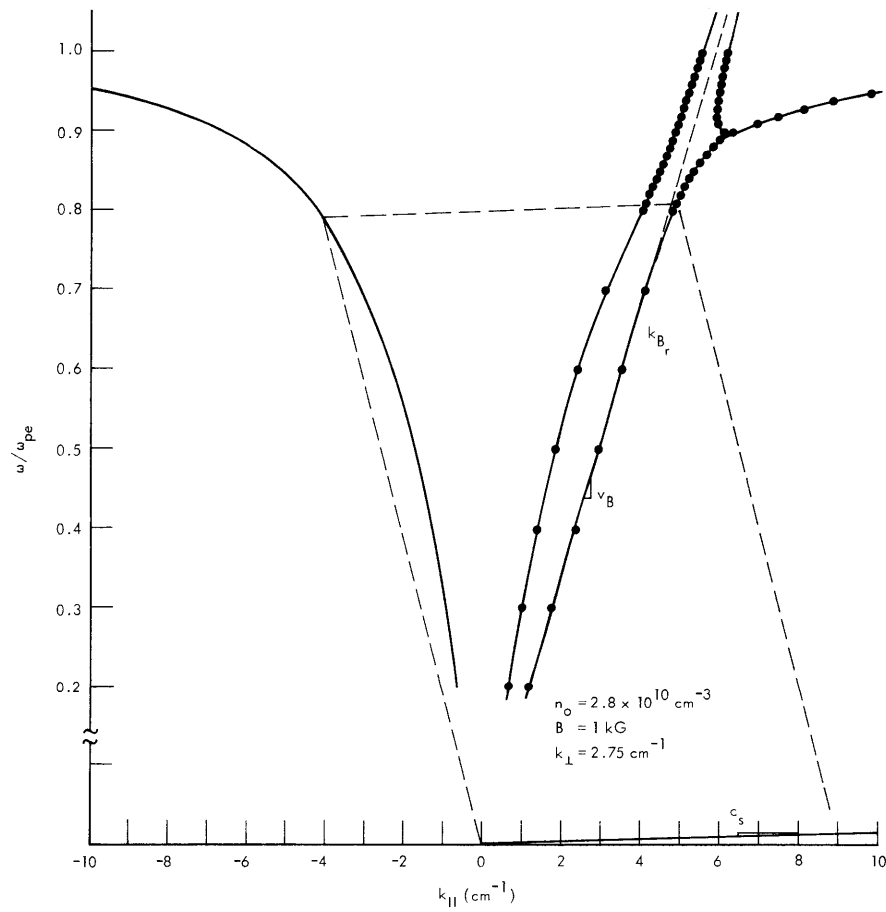
Schematic operation of an "up-converter."

Fig. XVI-9. GWDR showing a resonant interaction with the acoustic branch.
(Acoustic branch not to scale.)

is identical with that which occurs in an up-converter, as shown schematically in Fig. XVI-8. A signal at f_3 is parametrically amplified at a higher frequency f_2 (idler) with a gain of f_2/f_3. The energy is supplied by a pump wave at $f_p = f_2 + f_3$.

The pronounced peak in the low-frequency spectrum at ~450 kHz might also be explained by a parametric interaction if we consider the GWDR shown in Fig. XVI-9. If we assume that the LF spectrum does correspond to the acoustic branch, then a k_{res} is determined by $k_{res} = \dfrac{\omega_{res}}{c_s} = 9.0 \text{ cm}^{-1}$. Typically, wave numbers of the entrained beam wave are in the range $k_b \approx 4\text{-}5 \text{ cm}^{-1}$. Thus k-matching is possible only for a coupling between the forward acoustic mode and the backward plasma wave, as shown in Fig. XVI-9. Because of the bandlimited nature of the LF spectrum, k_{res} is essentially constant over a corresponding idler-wave spectrum. Therefore, only a single value of ω exists which will couple resonantly with the acoustic branch. Other values of ω will be driven off-resonance and thus give rise to the lower amplitude spectrum that is observed. The quantitative parameters predicted by this model, therefore, seem correct. Although the incoherent and broadband nature of the beam-excited LF spectrum makes standard interferometry difficult, we are attempting other techniques to identify the waves and processes involved. We wish to point out, however, that other beam-related processes may be responsible; for example, a change in equilibrium configuration or current-driven instability induced by the beam.

Mode-Coupled Interaction

To study mode-coupled interactions, two HF waves were excited in the plasma. One wave was the entrained beam wave which we have discussed. The second wave was
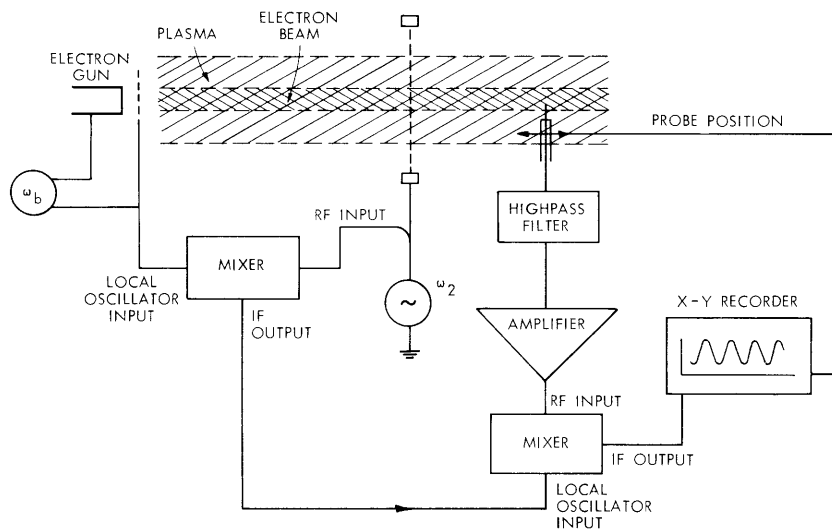

Fig. XVI-10. Mode-coupled experiment.

excited by applying several watts of RF power to a wire grid in the plasma. These two waves can then be expected to drive a difference-frequency wave, even if it is not a natural mode of the plasma. The interaction will be strongest, however, if the difference ω and k do correspond to a natural plasma mode. Figure XVI-10 is a schematic diagram of this experiment. Samples from the HF oscillators are mixed, and the difference frequency is used to measure the wavelength of the LF wave.

Figure XVI-11 is a spectrum analyzer display of the LF wave. The frequency of this wave corresponds to the frequency difference between the oscillators, and can be
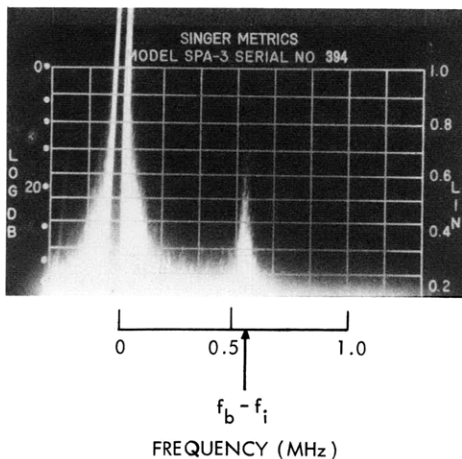
Fig. XVI-11.

Low-frequency spectrum showing wave excited by two HF fields.

tuned accordingly. Wavelength measurements were often complicated by the presence of the beam-excited acoustic spectrum. To prevent this, sufficient helium was added to the vacuum chamber to Landau-damp the spectrum. The nonlinear interaction, however, is strong enough to remain essentially unaffected by the small change in damping rate. Simple three-wave coupling theory for two constant HF pumps predicts that the excited wave amplitude should be proportional to the "idler" wave amplitude. This is confirmed experimentally as shown in Fig. XVI-12.

The result of an experimental dispersion analysis is shown in Fig. XVI-13. The wavelength of the LF wave is constant over the full range of the interaction. The wave amplitude, however, shows a pronounced resonance at a frequency which corresponds to a phase velocity equal to the sound speed in the plasma. While the LF wave is driven off-resonance from the acoustic branch, the wave amplitude remains constant. When the HF waves can interact resonantly with the acoustic branch, however, the wave amplitude increases significantly and displays a very sharp resonance.

Additional data revealed that the wavelength of the entrained beam wave was equal to that of the LF wave. This implies that the wave number of the idler wave must be zero. This suggests that our wire grid is exciting an electrostatic field that has a
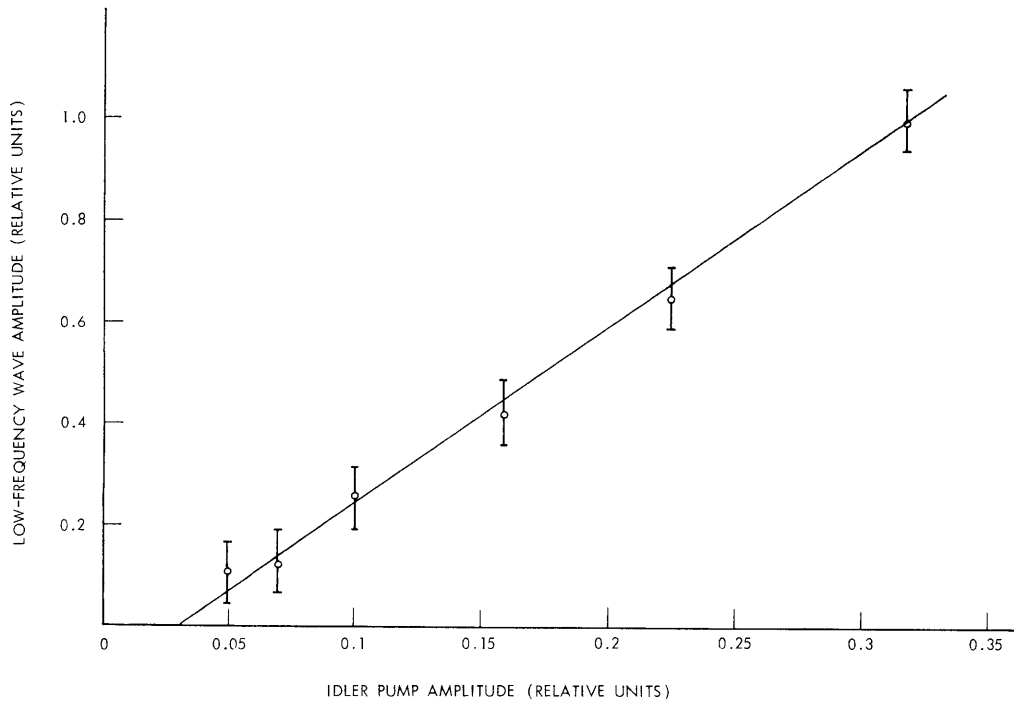
Fig. XVI-12. Amplitude of difference-frequency wave vs amplitude of pump field.
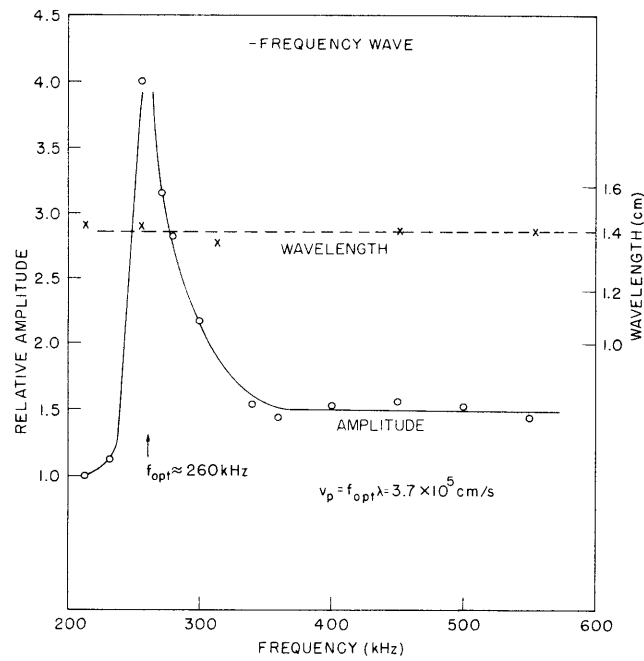
Fig. XVI-13. Amplitude and wavelength dependence of IF wave vs frequency difference of HF fields.

resonant cone structure.[4,5] Such a field exists only along a specific angle to the mag-
netic field. At all points along this angle, the field is in phase and exhibits essentially
infinite wavelength. It is not really surprising that our grid excites this type of field,
since the geometry is very similar to that used by Simonutti, Parker, and Briggs.[5] This
explanation is also supported by the lack of any detectable wavelength associated with
the idler wave, and the fact that the interaction strength is a function of radial position
and extends over a sharply defined axial length.
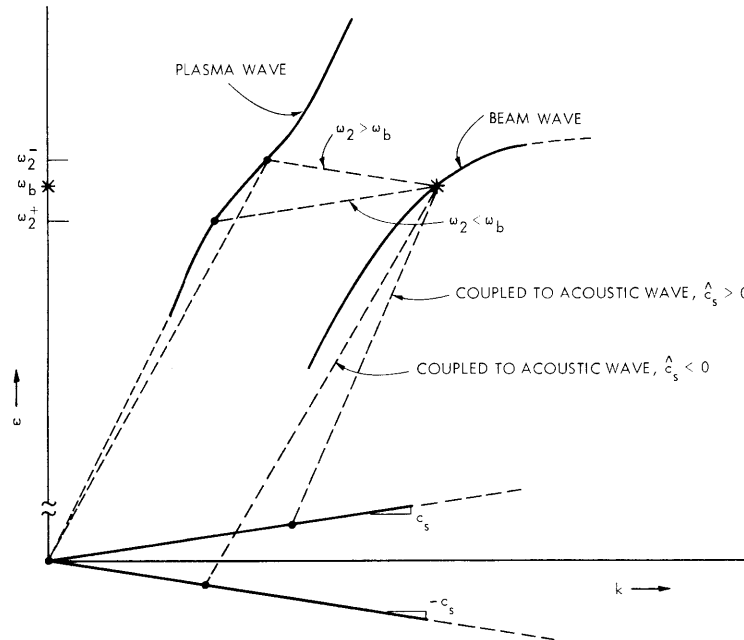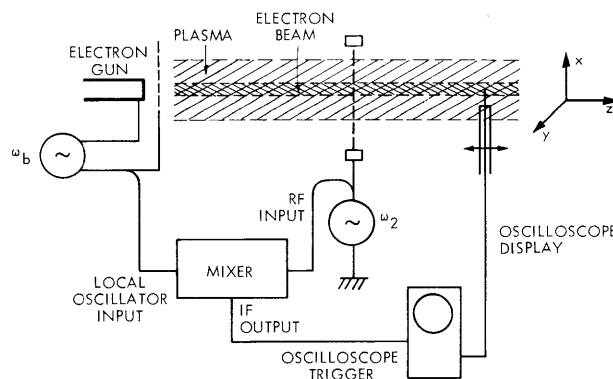
Fig. XVI-14. (a) Possible interactions with acoustic wave for $c_s > 0$ and $c_s < 0$.
(b) Experiment for measuring direction of wave propagation.

The magnitude of the two HF fields is approximately equal during this mode-coupled interaction. We can therefore expect the LF wave to be excited if the frequencies of the HF waves are exchanged. Of course, the specific characteristics of the interaction may change. Figure XVI-14a demonstrates this schematically. Here a beam wave and general plasma mode (or dipole field) have resonantly coupled with the acoustic branch. The diagram indicates how the two waves could interact with either of the oppositely directed acoustic waves. This effect has been observed experimentally, as shown in Fig. XVI-14b. The frequency difference between the oscillators is used as a reference
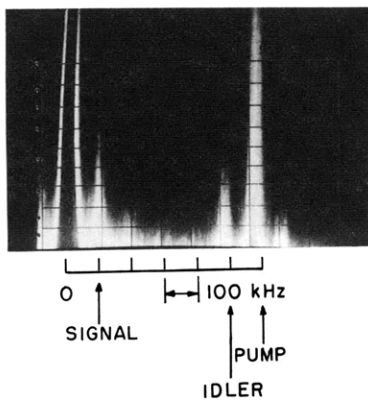
Fig. XVI-15.

Low-frequency parametric interaction driven by another mode-coupled interaction.

to measure the direction of phase shift of the LF wave as the receiving probe is moved axially. We find, in agreement with our predictions, that

$$\hat{c}_s = \hat{v}_b \qquad \text{for } \omega_2 < \omega_b$$

$$\hat{c}_s = -\hat{v}_b \qquad \text{for } \omega_2 > \omega_b.$$

Finally, we offer Fig. XVI-15 as evidence of the strength of the observed mode-coupled interaction. Again, two HF waves were used to excite an LF wave at 600 kHz. In this case, however, the excited wave is sufficiently strong so that the difference wave parametrically itself excites another lower frequency wave (perhaps a drift wave) at ~100 kHz, as well as an energy-matching idler sideband. Although this photograph is not typical, it is perhaps the best evidence that the excited LF wave is indeed a strong, coherent, and well-defined plasma wave.

We acknowledge the contribution of Professor R. J. Taylor who suggested the contaminant Landau damping and P. Widing, whose computer code was used in the numerical evaluation of the GWPR.

References

1. A. Y. Wong et al., in IAEA/CN-28, Proc. Fourth Conference on Plasma Physics and Controlled Nuclear Fusion Research, International Atomic Energy Agency, University of Wisconsin, Madison, Wisconsin, June 17-23, 1971.

2. R. J. Briggs, Electron-Stream Interaction with Plasma (The M. I. T. Press, Cambridge, Mass., 1964).

3. A. Bers, M. I. T. Course 6.58 Notes, Fall 1971 (unpublished).

4. R. Fisher and R. Gould, Phys. Fluids 14, 857-867 (1971).

5. M. Simonutti, R. R. Parker, and R. J. Briggs, Quarterly Progress Report No. 104, Research Laboratory of Electronics, M. I. T., January 15, 1972, pp. 196-201.

2. ANALYTIC STUDIES OF NONLINEAR PLASMA PROBLEMS BY SYMBOLIC MANIPULATION PROGRAMS ON A COMPUTER

A. Bers, J. L. Kulp, D. C. Watson

Introduction

The simulation of charged-particle dynamics on a computer has greatly increased our understanding of strongly nonlinear (in particular, nonlaminar) phenomena in plasmas. Such simulations are impractical for studying nonlinear phenomena whose time and space scale of evolution is many orders of magnitude larger than the individual particle dynamics scales. Examples of such phenomena are the weakly nonlinear (either coherent or turbulent) wave interactions in a plasma, and most of the phenomena associated with the nonlinear (but laminar) fluid dynamics behavior of plasmas such as occur in studies of transport properties and equilibrium configurations. In contrast to particle simulations which require a large number of numerical computations, weakly nonlinear phenomena can best be studied by perturbation techniques that require a large number of symbolic computations. Recent advances in the development of symbolic manipulation programs now make it possible to build up and implement on a computer analytic techniques suitable for solving nonlinear dynamics problems.

During the past year, in cooperation with the MATHLAB Group of M. I. T.'s Project MAC, we have initiated such an implementation. Our first focus is a study of the non-linear wave interactions in the fluid model of a plasma in a magnetic field. All of the work is being carried out on the Project MAC Symbol Manipulating system called MACSYMA (see Fig. XVI-16). This is a hierarchical, evolving computer system with specific capabilities for symbolic manipulation of algebraic expressions and mathematical operations. A detailed description of this system appears in the "Proceedings of the Second Symposium on Symbolic and Algebraic Manipulation" (March 1971).[1] These
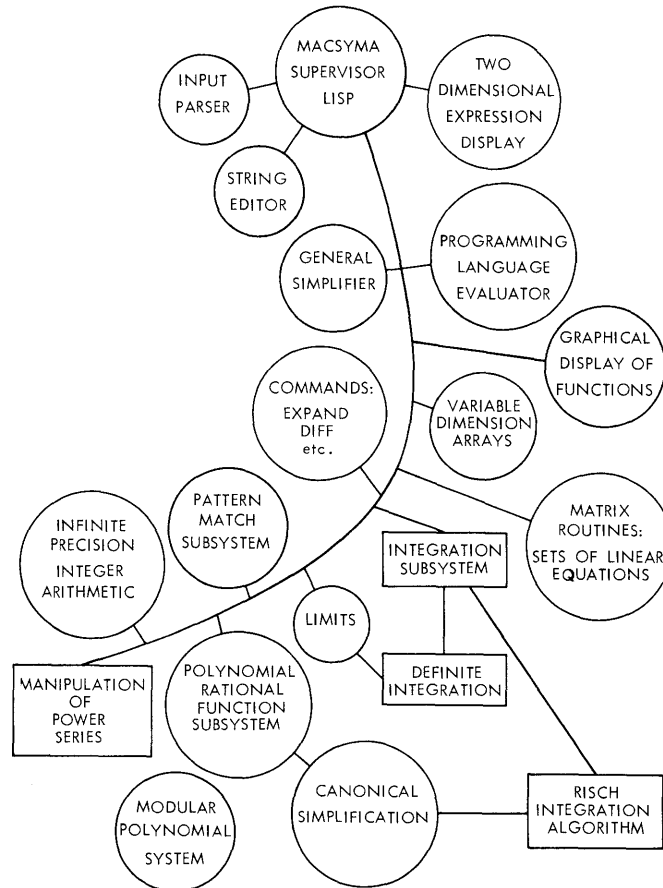
Fig. XVI-16. MACSYMA system.

proceedings also provide a useful overview of this computer field.

In this first report we present a brief description with illustrations of various analytical capabilities of MACSYMA, and show the use of this system in the study of nonlinear wave interactions in plasmas.

General Description of MACSYMA

MACSYMA is a symbol-manipulation system in which various mathematical operations can be carried out in analytic form. A symbolic manipulation system is one in which inputs are expressions or equations in symbolic form. Mathematical operations are carried out on these expressions, and answers are returned in a two-dimensional display of symbolic mathematical form. This system is useful for obtaining analytic solutions to problems, as opposed to the conventional numerical analysis for which computers have been more commonly employed. The ability to interact with a derivation and control its progress is very important. Thus the basic mode of operations of MACSYMA is conversational; it is implemented on a time-sharing computer system (DEC-PDP 10).

Many of the interesting capabilites are briefly discussed in this report, with simple examples given which are intended to illustrate the meaning of features rather than their power in handling realistic problems.

a. Expression Manipulation

This type of command includes strictly algebraic operations encountered in symbolic manipulations. Examples of expression manipulation are shown in Fig. XVI-17.

1. Simplification. Finding expressions which reduce to zero or one; canceling common factors; simplifying special cases as in trigonometric functions, noncommutative multiplication, matrices, and calculus operators.

2. Expanding expressions.

3. Extracting parts of an expression; taking coefficients; taking real and imaginary parts.

4. Substitution; substituting for extracted parts.

5. Factoring over the fields of integers, Gaussian integers (integers $\times \sqrt{-1}$), and some algebraic numbers.

6. Polynomial manipulation; raising to a power; division; partial fraction and continued-fraction expansions.

b. Evaluation

Evaluation can be either numerical or symbolic. An example of symbolic evaluation is the following. Let A be assigned the value B+C. This is A:B+C in MACSYMA notation. If we then input EVALUATE (A^2), we get $(B+C)^2$. Numerical evaluation is illustrated by the following. A:$\pi/4$, EVALUATE ($\sin^2 A$, NUMER); the return is 1/2. This capability is important because once an expression is derived symbolically, there is no need to write a computer program to evaluate it numerically. The expression is, in a sense, already programmed in the system.

c. Matrix Manipulation

All standard vector-matrix operations are available: transpose, inverse, matrix multiplication, determinant, characteristic polynomial, extraction of a coefficient matrix from a set of equations, differentiation, integration, and any other operation that can be applied to an ordinary scalar expression. Examples of matrix manipulation are shown in Fig. XVI-18. Extensive array and list structure capability is included.

d. Calculus

Most standard calculus operations are available. Examples of calculus operations are shown in Fig. XVI-19.

1. Differentiation — total or partial derivatives, and special gradient definitions.

Explanation: The Ci lines are commands or expressions typed by the user,
while the Di lines are the computer responses. "@" terminates a command.
"$" stands for the last expression mentioned (i.e. the last Ci or Di line).
The " ´ " character indicates that a function or command is to be displayed
but not evaluated or carried out. Also the command EXPR,EXPAND is equiv-
alent to EXPAND(EXPR). RATSIMP is a command which tries to put expressions
in a ratio-of-polynomials form and also does simplification.

SIMPLIFICATION EXAMPLE:

Note that simplification is automatically invoked at the end of any operation.

(C1) A + (X*B+B*(A/B−X)) @

$$(D1) \qquad\qquad B\ (\frac{A}{B} - X) + B\ X + A$$

(C2) RATSIMP(D1)@

$$(D2) \qquad\qquad\qquad 2\ A$$

Here, the simplifier has noticed that −BX + BX is equivalent to 0 and A+A is 2A.

EXPANSION EXAMPLE:

The EXPAND command carries out distribution of operators such as multiplication
(and some linear and bilinear operators), as well as, matrix multiplications.
Many options are available to control the extent of expansion.

(C1) EXPAND((A+B)**4)@

$$(D1) \qquad B^4 + 4\ A\ B^3 + 6\ A^2\ B^2 + 4\ A^3\ B + A^4$$

(C2) EXPAND((X+Y)**2*(A+B)**2)@

$$(D2)\ B^2\ Y^2 + 2\ A\ B\ Y^2 + A^2\ Y^2 + 2\ B^2\ X\ Y + 4\ A\ B\ X\ Y + 2\ A^2\ X\ Y$$

$$+\ B^2\ X^2 + 2\ A\ B\ X^2 + A^2\ X^2$$

Now consider an example of rationally simplifying and factoring expanded expressions.

(C3) D1/D2@

$$(D3)\ (B^4 + 4\ A\ B^3 + 6\ A^2\ B^2 + 4\ A^3\ B + A^4)$$

$$/(B^2\ Y^2 + 2\ A\ B\ Y^2 + A^2\ Y^2 + 2\ B^2\ X\ Y + 4\ A\ B\ X\ Y + 2\ A^2\ X\ Y + B^2\ X^2$$

$$+\ 2\ A\ B\ X^2 + A^2\ X^2)$$

(C4) FACTOR(RATSIMP(D3))@

$$(D4) \qquad\qquad \frac{(B + A)^2}{(Y + X)^2}$$

RATSIMP has canceled out the factor (A+B)**2 which is not easily seen in D3.

An example of expanding the integrate operator.

(C5) ´INTEGRATE(A*F(X)+B*G(X),X,MIN,INF)@

$$(D5) \qquad\qquad \int_{MIN}^{INF} (B\ G(X) + A\ F(X))\ DX$$

(C6) DECLARE(INTEGRATE,LINEAR)$

(C7) D5,EXPAND@

$$(D7) \qquad\qquad B\ (\int_{MIN}^{INF} G(X)\ DX) + A\ (\int_{MIN}^{INF} F(X)\ DX)$$

Fig. XVI-17.   Examples of commands for general expression manipulation.

EXTRACTION OF PARTS EXAMPLE:

To extract the 4 th term in the denominator of D3, first "circle" it to see
if that is the term we want, and then extract it.

(C8) DPART(D3,2,4)@

(D8) $(B^4 + 4 A B^3 + 6 A^2 B^2 + 4 A^3 B + A^4)$

$$/(B^2 Y^2 + 2 A B Y^2 + A^2 Y^2 + \overset{**********}{\underset{**********}{* 2 B X Y *}} + 4 A B X Y + 2 A^2 X Y$$

$$+ B^2 X^2 + 2 A B X^2 + A^2 X^2)$$

(C9) PART(D3,2,4)@

(D9) $2 B^2 X Y$

To extract rational coefficients, RATCOEF is used. Here the coefficient
of A**4 in (A+B)**8 is found.

(C11) RATCOEF((A+B)**8,A**4)@

(D11) $70 B^4$

(C12) (X+A)*(Y+3)**2-(X+A)*COS(A)**2-(Y+C)**3=0@

(D12) $- (Y + C)^3 + (X + A) (Y + 3)^2 - COS^2(A) (X + A) = 0$

(C13) EXPAND(%)@

(D13) $- Y^3 + X Y^2 - 3 C Y^2 + A Y^2 + 6 X Y - 3 C^2 Y + 6 A Y - COS^2(A) X + 9 X - C^3$

$$- A COS^2(A) + 9 A = 0$$

(C14) RATCOEF(LHS(%),X+A)@

(D14) $Y^2 + 6 Y - COS^2(A) + 9$

Note the the left-hand-side operator had to be used, since equations
are not rational expressions. The coefficient of X+A is not evident in D13.
The use of RATCOEF and RATSUBST (below) makes it possible to control the size
and form of expressions.

Taking real and imaginary parts is illustrated below. %E is the base of the
natural logs, and %I is the sqrt(-1)

(C15) %E**(%I*ANGLE)@

(D15) $\%E^{\%I \ ANGLE}$

(C16) REALPART(%)@
(D16) $COS(ANGLE)$

(C17) (A+%I*B)/(D+%I*E)@

(D17) $\dfrac{\%I B + A}{\%I E + D}$

(C18) IMAGPART(%)@

(D18) $\dfrac{B D}{E^2 + D^2} - \dfrac{A E}{E^2 + D^2}$

(C19) RATSIMP(D18)@

(D19) $- \dfrac{A E - B D}{E^2 + D^2}$

Fig. XVI-17. (continued)

SUBSTITUTION EXAMPLES:

The substitution for extracted parts is illustrated.
First, consider substituting W[PE]**2*EP[O] for Q**2*NO/M .

(C1) Q**2*NO*E/M/SI/W@

(D1)
$$- \frac{SI \ E \ NO \ Q^2}{M \ W}$$

(C2) RATSUBST(W[PE]**2*EP[O],Q**2*NO/M,%)@

(D2)
$$- \frac{SI \ EP_O \ E \ W_{PE}^2}{W}$$

(C3) (X+A)*(Y+3)**2-(X+A)*COS(A)**2-(Y+C)**3=0@

(D3)
$$- (Y + C)^3 + (X + A) (Y + 3)^2 - \cos^2(A) (X + A) = 0$$

(C4) EXPAND(%)@

(D4)
$$- Y^3 + X Y^2 - 3 C Y^2 + A Y^2 + 6 X Y - 3 C^2 Y + 6 A Y - \cos^2(A) X + 9 X - C^3$$
$$- A \cos^2(A) + 9 A = 0$$

In this example RATSUBST must effectively extract the factor X+A and
then substitute XFAC for it.

(C5) RATSUBST(XFAC,X+A,LHS(D4))@

(D5)
$$- Y^3 + (XFAC - 3 C) Y^2 + (6 XFAC - 3 C^2) Y - \cos^2(A) XFAC + 9 XFAC - C^3$$

The RAT command reorders the expression with XFAC as the most important variable.

(C6) RAT(%,XFAC)@

(D6)
$$(Y^2 + 6 Y - \cos^2(A) + 9) XFAC - Y^3 - 3 C Y^2 - 3 C^2 Y - C^3$$

It should be noted that RATSUBST sometimes has strange effects when substituting
for a simple factor such as Y+C.

FACTORING EXAMPLE:

An interesting factoring problem.

(C1) X**99+1

(D1)
$$X^{99} + 1$$

(C2) FACTOR(%)

(D2) $(X + 1) (X^2 - X + 1) (X^6 - X^3 + 1) (X^{10} - X^9 + X^8 - X^7 + X^6 - X^5 + X^4 - X^3 + X^2 - X$
$+ 1) (X^{20} + X^{19} - X^{17} - X^{16} + X^{14} + X^{13} - X^{11} - X^{10} - X^9 + X^7 + X^6 - X^4 - X^3 + X + 1)$
$(X^{60} + X^{57} - X^{51} - X^{48} + X^{42} + X^{39} - X^{33} - X^{30} - X^{27} + X^{21} + X^{18} - X^{12} - X^9 + X^3 + 1)$

Fig. XVI-17. (continued)

PARTIAL FRACTION EXPANSION EXAMPLE:

(C1) (X+2)/(X+3)/(X+B)/(X+C)**2@

(D1)
$$\frac{X + 2}{(X + 3) (X + B) (X + C)^2}$$

This shows the main use of RATSIMP - to put expressions in ratio-of-polynomials form. The most important variable is assumed to be X.

(C2) RATSIMP(%)@

(D2) $(X + 2)/(X^4 + (2 C + B + 3) X^3 + (C^2 + (2 B + 6) C + 3 B) X^2$
$$+ ((B + 3) C^2 + 6 B C) X + 3 B C^2)$$

Now take a partial fraction expansion of this ratsimped expression. The answer would be the same as if we had expanded D1 directly, but it is less obvious from this form.

(C3) PARTFRAC(%,X)@

(D3) $-((C^2 - 4 C - B + 6) X + 2 C^3 + (- B - 9) C^2 + (4 B + 12) C - 6 B)$

$/((C^4 + (- 2 B - 6) C^3 + (B^2 + 12 B + 9) C^2 + (- 6 B^2 - 18 B) C + 9 B^2) X^2$

$+ (2 C^5 + (- 4 B - 12) C^4 + (2 B^2 + 24 B + 18) C^3 + (- 12 B^2 - 36 B) C^2 + 18 B^2 C) X$

$+ C^6 + (- 2 B - 6) C^5 + (B^2 + 12 B + 9) C^4 + (- 6 B^2 - 18 B) C^3 + 9 B^2 C^2)$

$+ (B - 2)/(((B - 3) C^2 + (6 B - 2 B^2) C + B^3 - 3 B^2) X + (B^2 - 3 B) C^2$

$+ (6 B^2 - 2 B^3) C + B^4 - 3 B^3)$

$- 1/(((B - 3) C^2 + (18 - 6 B) C + 9 B - 27) X + (3 B - 9) C^2 + (54 - 18 B) C + 27 B$

$- 81)$

This does not look like a partial fraction expansion because factors have been multiplied out. To see this we use a function we have written in MACSYMA which factors terms in a sum and subexpressions. It can now be seen that the factors have been expanded above.

(C4) FACTERMS(%)@

(D4) $\dfrac{B - 2}{(B - 3) (C - B)^2 (X + B)} - \dfrac{1}{(B - 3) (C - 3)^2 (X + 3)}$

$$- \frac{(C^2 - 4 C - B + 6) X + 2 C^3 + (- B - 9) C^2 + 4 (B + 3) C - 6 B}{(C - 3)^2 (C - B)^2 (X + C)^2}$$

Now we refactor to obtain the original result.

(C5) FACTOR(%)@

(D5)
$$\frac{X + 2}{(X + 3) (X + B) (X + C)^2}$$

SUMMARY: It is important to notice how these commands can be used to reduce the complexity of expressions and for restructuring them in a desirable form. Also, as in the factoring case, simplifying procedures can lead to unwanted results which are larger than what was started with. By interacting with expressions, these problems can be avoided.

Fig. XVI-17. (concluded)

EXAMPLES OF MATRIX OPERATIONS:

The first example is taking the inverse of a matrix which occurs in the cold plasma theory (resulting in the mobility tensor). (G)**(-1) is taking the inverse of D1. " :" means "assign to".

(C1) INVERSEMODG

(D1)
$$\begin{bmatrix} \%I\ W & -\ WC & 0 \\ WC & W\ \%I & 0 \\ 0 & 0 & W\ \%I \end{bmatrix}$$

(C2) MAT:EV((G)**(-1),RATSIMP);

(D2)
$$\begin{bmatrix} \dfrac{\%I\ W}{WC^2 - W^2} & \dfrac{WC}{WC^2 - W^2} & 0 \\ -\dfrac{WC}{WC^2 - W^2} & \dfrac{\%I\ W}{WC^2 - W^2} & 0 \\ 0 & 0 & -\dfrac{\%I}{W} \end{bmatrix}$$

The ALIAS command is used for abreviating long names.

(C3) ALIAS(CC,COMPLEXCONJ,TT,TRANSPOSE);

Below several matrix operations are illustrated including multiplication and differentiation. The example is the calculation of the time averaged energy in the linear modes of a cold plasma. W is frequency, EP[0] is the free space dielectric constant. "*" as a superscript indicates complexconjugate. Note that the answer is in an awkward form. This is a general problem of symbolic manipultion systems.

(C4) EPSILON(W):=EP[0]*IDENT(3) + WPE**2*EP[0]*"MAT/%I/W;

(D4) EPSILON(W) := EP_0 IDENT(3) $-$

$$\dfrac{\%I\ EP_0\ WPE^2 \begin{bmatrix} \dfrac{\%I\ W}{WC^2 - W^2} & \dfrac{WC}{WC^2 - W^2} & 0 \\ -\dfrac{WC}{WC^2 - W^2} & \dfrac{\%I\ W}{WC^2 - W^2} & 0 \\ 0 & 0 & -\dfrac{\%I}{W} \end{bmatrix}}{W}$$

(C5) CC(TT(E1)).'DIFF(EPSILON(W),W).E1/4;

(D5)

$$\dfrac{\begin{bmatrix} E_X & E_Y & E_Z \end{bmatrix} \cdot \left(\left(\dfrac{EP_0}{W} \begin{bmatrix} 1 & 0 & 0 \\ 0 & 1 & 0 \\ 0 & 0 & 1 \end{bmatrix} - \dfrac{\%I\ EP_0\ WPE^2 \begin{bmatrix} \frac{\%I\ W}{WC^2 - W^2} & \frac{WC}{WC^2 - W^2} & 0 \\ -\frac{WC}{WC^2 - W^2} & \frac{\%I\ W}{WC^2 - W^2} & 0 \\ 0 & 0 & -\frac{\%I}{W} \end{bmatrix}}{W} \right) \right) \cdot \begin{bmatrix} E_X^* \\ E_Y^* \\ E_Z^* \end{bmatrix}}{4}$$

(C6) FACTOR(EV(%,DIFF,EXPAND));

(D6) $(EP_0\ WPE^2\ (W^4\ (2\ E_Z\ E_Z^* + 2\ E_Y\ E_Y^* + 2\ E_X\ E_X^*) + 2\ WC^4\ E_Z\ E_Z^* - 4\ W^2\ WC^2\ E_Z\ E_Z^*$

$+ \%I\ W^3\ WC\ (3\ E_X\ E_Y^* - 3\ E_X^*\ E_Y) + \%I\ W\ WC^3\ (E_Y\ E_X^* - E_X\ E_Y^*)))$

$/(2\ W^3\ (WC + W)^2\ (WC - W)^2)$

Fig. XVI-18.   Examples of matrix operations.

EXAMPLES OF CALCULUS OPERATIONS:

Below are examples of the DIFF command which carries out differentiations.

(C1) X^2*SIN(X)+Y*X+%E**(X^2)/X+COSH(X)@

(D1)
$$X Y + X^2 SIN(X) + COSH(X) + \frac{\%E^{X^2}}{X}$$

(C2) DIFF(D1,X)@

(D2)
$$Y + 2 X SIN(X) + X^2 COS(X) + SINH(X) - \frac{\%E^{X^2}}{X^2} + 2 \%E^{X^2}$$

The period operator "." is noncommutative multiplication which can be used for vector or matrix multiplication or for defining operators such as "GRAD." . Note that A,B,C,D must depend on t.

(C3) A.B+C.D@

(D3)
$$C . D + A . B$$

(C4) DIFF(D3,T)@

(D4)
$$\frac{DC}{DT} . D + C . \frac{DD}{DT} + \frac{DA}{DT} . B + A . \frac{DB}{DT}$$

Here the special gradient definition feature is shown. The derivative of $g(x)$ is defined as $g'(x)$.

(C5) GRADEF(G(X),?G'?(X))@
(D5)
$$G$$

(C6) 'DIFF(G(X),X) = DIFF(G(X),X)@

(D6)
$$\frac{D}{DX} G(X) = G'(X)$$

Fig. XVI-19. Examples of integration in MACSYMA.

An example of indefinite real domain integration with verification of results.

(C7) INTEGRATE(1/(X**3+A**3),X)

(D7)
$$\int \frac{1}{X^3 + A^3}\, DX$$

(C8) EV(%,INTEGRATE)

(D8)
$$-\frac{LOG(X^2 - A\,X + A^2)}{6\,A^2} + \frac{ATAN\left(\frac{2\,X - A}{SQRT(3)\,A}\right)}{SQRT(3)\,A^2} + \frac{LOG(X + A)}{3\,A^2}$$

(C9) DIFF(%,X,1)

(D9)
$$\frac{2}{3\,A^3\left(\frac{(2\,X - A)^2}{3\,A^2} + 1\right)} - \frac{2\,X - A}{6\,A^2\,(X^2 - A\,X + A^2)} + \frac{1}{3\,A^2\,(X + A)}$$

(C10) RATSIMP(%)

(D10)
$$\frac{1}{X^3 + A^3}$$

Consider a complex contour integral that occurs in plasma problems.

(C1) N1(W,K)/NO=Q*E(W,K)/M*'INTEGRATE('DIFF(F[O](V),V)/%I/(W-K*V),V,MINF,INF)@

(D1)
$$\frac{N1(W,\ K)}{NO} = \frac{Q\ E(W,\ K)\ \left(\int_{MINF}^{INF}\left(-\frac{\%I\left(\frac{D}{DV}F_0(V)\right)}{W - K\ V}\right)DV\right)}{M}$$

Evaluate this integral for f0(v) a Lorentian distribution. Note w must have an imaginary part since the integration command drops the imaginary part of real integrals.

(C2) %,F[O](V)=A/%PI/(V^2+A^2),W=WR+%I*WI,DIFF@

(D2)
$$\frac{N1(WR + \%I\ WI,\ K)}{NO} = \frac{Q\ E(WR + \%I\ WI,\ K)\ \left(\int_{MINF}^{INF}\frac{2\ \%I\ A\ V}{\%PI\ (V^2 + A^2)^2\ (WR + \%I\ WI - K\ V)}\,DV\right)}{M}$$

(C3) T,T=EV(%,INTEGRATE),WR=W,WI=0@

(D3)
$$\frac{N1(W,\ K)}{NO} = \frac{\%I\ K\ Q\ E(W,\ K)}{M\ (\%I\ W + A\ K)^2}$$

Fig. XVI-19. (continued)

Special operators such as GRAD, DIV, CURL can be implemented.

    2. Integration — indefinite integrals, definite integrals, complex contour integrals (residues), including some branch cut integrations. Integrals are actually worked out as opposed to being looked up in tables.[1]

e. Solution of Equations

    Capabilities available on MACSYMA are listed here; other techniques for special problems can be adapted from these.

    1. Solution of systems of linear algebraic equations.

    2. Solution (or at least partial elimination) of sets of nonlinear algebraic equations.

    3. Ordinary differential equations (also Laplace transforms).

    4. Solution of differential equations by power series methods.

    5. Solution of linear vector-matrix equations.

    6. Solution of some integral equations.

Examples of some of these are shown in Fig. XVI-20.

f. Summation, Indexed Products, Limits, Power Series

    Infinite or indefinite sums or products can be evaluated or manipulated. A powerful power series package is being implemented but has not yet been debugged. Taylor, Laurant, and user-written functional power series expansions are available. Examples are given in Fig. XVI-21.

g. Pattern Matching

    This feature allows a user to build new information into the system; vector identities, trigonometric identities, special functions (Bessel, Zeta — the plasma dispersion function, etc.), operators, and other useful conventions can be handled in this way.

h. Auxiliary Features

    System control commands, disk-file storage, string manipulation, programming, editing, plotting, graphing, input-output commands, aliases (abbreviations), debugging, association of names and properties, and display are included.

    In addition to the features mentioned, MACSYMA "knows about" complex variable algebra, trigonometric, hyperbolic, and exponential functions (including Arc functions), special values such as π, e, $\sqrt{-1}$, Bernoulli and Euler numbers. Also MACSYMA can do numerical calculations to any desired degree of accuracy (with a price paid in speed).

    Most of these features of MACSYMA are needed when the solution to a realistic problem is attempted, and the fact that it has so many sophisticated capabilities encourages us about the prospect of overcoming difficulties encountered with other algebraic manipulation systems. These difficulties arise, for the most part, because of the inability of

SOLUTION OF EQUATIONS EXAMPLES:

The solution of a set of 3 by 3 linear algeraic equations.

(C2) A*X+B*Y+C*Z=25

(D2)   C Z + B Y + A X = 25

(C3) 2*X+4*Y+8*Z=1

(D3)   8 Z + 4 Y + 2 X = 1

(C4) X+Z=0

(D4)   Z + X = 0

(C5) SOLVE([D2,D3,D4],[X,Y,Z])

SOLUTION

(E5) $X = \dfrac{B - 100}{4 C - 6 B - 4 A}$

(E6) $Y = \dfrac{C - A - 150}{4 C - 6 B - 4 A}$

(E7) $Z = -\dfrac{B - 100}{4 C - 6 B - 4 A}$

(D7)   [E5, E6, E7]

Below is an example of solving nonlinear algebraic equations. Several techniques are
used but basically the set of equations is put in a polynomial form where the main
variables in the polynomial are functions of the variables being solved. Then poly-
nomial solving techniques are used, and functions inverted. Also, sets of equations
are solved by elimination.

(C8) XS:X**2 - 12*X + 38

(C9) SIN(XS)**2-5*SIN(XS)+3

(D9) $SIN^2(X^2 - 12 X + 3) - 5 SIN(X^2 - 12 X + 3) + 3$

(C10) SOLVE(D,X)
SOLUTION

(E10) $X = 6 - SQRT(ASIN(- \dfrac{SQRT(13) - 5}{2}) + 33)$

(E11) $X = SQRT(ASIN(- \dfrac{SQRT(13) - 5}{2}) + 33) + 6$

(E12) $X = 6 - SQRT(ASIN(\dfrac{SQRT(13) + 5}{2}) + 33)$

(E13) $X = SQRT(ASIN(\dfrac{SQRT(13) + 5}{2}) + 33) + 6$

(D14)   [E10, E11, E12, E13]

This is an example of the solution of a first order ordinary differential
equation (Bernoulli equation). CONST is an integration constant.

(C15) X**2*(X-1)*'DIFF(Y,X) + Y**2 -X*(X-2)*Y

(D15) $X^2 (X - 1) \dfrac{DY}{DX} + Y^2 - X (X - 2) Y$

(C16) SOLDIFR(D)

(D16) $CONST = \dfrac{X^2}{(X - 1) Y} + \dfrac{1}{X - 1}$

(C17) SOLVE(D,Y)

(D17) $Y = \dfrac{X^2}{CONST (X - 1) - 1}$

Fig. XVI-20.   Examples of the solution of equations on MACSYMA.

EXAMPLES OF TAYLOR SERIES AND LIMITS:

Although there is a built in Taylor series command, consider, as an example of
programming in MACSYMA, a function written in the MACSYMA language which
computes Taylor series.

```
TAYLOR(EXPR,VAR,POINT,HIPOWER):=
    BLOCK ([RESULT],
        RESULT: SUBST(POINT,VAR,EXPR),
        FOR I:1 THRU HIPOWER
            DO [EXPR: DIFF(EXPR,VAR) / I,
                RESULT: RESULT + (VAR - POINT)^I * SUBST(POINT,VAR,EXPR)],
        RETURN(RESULT))$
```

As a simple example of Taylor series expansions, consider the expansion of SIN(X)/X
in X about XO to third order.

(C1) TAYLOR(SIN(X)/X,X,XO,3)$

$$
(D1) \quad \frac{(X - XO)^2 \left(-\dfrac{SIN(XO)}{XO} + \dfrac{2\,SIN(XO)}{XO^3} - \dfrac{2\,COS(XO)}{XO^2} \right)}{2}
$$

$$
+ \frac{(X - XO)^3 \left(\dfrac{3\,SIN(XO)}{XO^2} - \dfrac{6\,SIN(XO)}{XO^4} - \dfrac{COS(XO)}{XO} + \dfrac{6\,COS(XO)}{XO^3} \right)}{6} + (X - XO)
$$

$$
\left(\frac{COS(XO)}{XO} - \frac{SIN(XO)}{XO^2} \right) + \frac{SIN(XO)}{XO}
$$

Consider the evaluation of this expression for XO = $PI/2 where $PI is pi.

(C2) %,XO=$PI/2$

$$
(D2) \quad \frac{\left(-\dfrac{96}{\$PI^4} + \dfrac{12}{\$PI^2} \right) \left(X - \dfrac{\$PI}{2} \right)^3}{6} + \frac{\left(\dfrac{16}{\$PI^3} - \dfrac{2}{\$PI} \right) \left(X - \dfrac{\$PI}{2} \right)^2}{2} - \frac{4 \left(X - \dfrac{\$PI}{2} \right)}{\$PI^2} + \frac{2}{\$PI}
$$

Now consider taking the infinite magnetic field limit of the mobility tensor for
a cold plasma. This is done by taking the limit as WC goes to infinity.

(C3) 'LIMIT(MAT,WC,INF)$

$$
(D3) \quad \lim_{WC \to INF}
\begin{bmatrix}
\dfrac{\$I\,W}{WC^2 - W^2} & \dfrac{WC}{WC^2 - W^2} & 0 \\[3ex]
-\dfrac{WC}{WC^2 - W^2} & \dfrac{\$I\,W}{WC^2 - W^2} & 0 \\[3ex]
0 & 0 & -\dfrac{\$I}{W}
\end{bmatrix}
$$

(C4) %,LIMIT$

$$
(D4) \quad
\begin{bmatrix}
0 & 0 & 0 \\
0 & 0 & 0 \\
0 & 0 & -\dfrac{\$I}{W}
\end{bmatrix}
$$

Fig. XVI-21.   Example of series expansions and limits.

controlling the size and form of expressions resulting from a derivation. While this is still a problem, MACSYMA has given the user several representations for expressions and some powerful commands for controlling the evolution of an expression through a calculation. Furthermore, advanced simplification and factoring techniques aid in reducing the size of expressions. The features and capabilities of MACSYMA have been described in greater detail elsewhere.[1, 2]

Use of the MACSYMA System in the Analysis of Nonlinear Wave Interactions in Plasmas

The initial problem that we are solving on MACSYMA is the derivation and evaluation of coupling coefficients describing the nonlinear coherent three-wave interactions in a plasma.[3] This coupling can be formulated as arising from the nonlinear current, which is given to second order in the electric field amplitude by

$$J_{2i} = \sigma_{ijk}^{ab} E_j^a E_k^b, \tag{1}$$

where the summation convention is used, and $\bar{E}^a$, $\bar{E}^b$ are the electric fields of all possible linear modes (indicated by superscripts), and $\bar{\bar{\sigma}}^{ab}$ is a third-rank tensor embodying the second-order nonlinear properties of the plasma. Once an expression for this current is found, evaluation of the coupling coefficients of the linear modes is straightforward. The coupling coefficient for the linear mode[2] is proportional to

$$\bar{E}^{n*} \cdot \bar{J}_2 = \sigma_{ijk}^{nab} E_i^{n*} E_j^a E_k^b. \tag{2}$$

Since we are primarily interested in the perburbation of the complex amplitudes of the linear modes, we consider the quantity $M^{nab} = \sigma_{ijk}^{nab} e_i^{n*} e_j^a e_k^b$ with e representing unit vectors (polarization) associated with the linear modes. We are exploring the use of MACSYMA in the derivation and then evaluation of M^{nab}. These two steps are rather distinct and will be discussed individually.

a. Derivation of $\bar{J}_2$

As a specific example to illustrate the general method, consider the derivation of $\bar{J}_2$ for a warm fluid plasma model. Note that it is sufficient to consider a single species because nonlinear conductivities for different species can be simply summed. To start, we type the following set of equations into MACSYMA:

$$\text{Force equation:} \quad n\,m\left[\frac{\partial}{\partial t}\bar{v} + (\bar{v}\cdot\bar{\nabla})\bar{v}\right] = -\nabla P + nq[\bar{E} + \bar{v}\times\bar{B}] \tag{3}$$

Continuity: $\qquad \dfrac{\partial n}{\partial t} + \overline{\nabla} \cdot (n\overline{v}) = 0$ (4)

Equation of state: $\quad P = P_O \left(\dfrac{n}{n_O}\right)^{\gamma}$ (5)

Faraday's law: $\quad \overline{\nabla} \times \overline{E} = -\dfrac{\partial \overline{B}}{\partial t}.$ (6)

Also, the relation $\overline{J} = qn\overline{v}$ is needed.

In order to arrive at a simple physical interpretation to a particular nonlinear wave interaction, we would like to be able to identify the terms in the fluid equations which give rise to the coupling. If the force equation is divided by n, it is evident that the following nonlinear terms occur in these equations.

1. $(\overline{v} \cdot \overline{\nabla}) \overline{v}$ $\qquad$ convective nonlinearity

2. $\overline{v} \times \overline{B}$ $\qquad$ Lorentz nonlinearity

3. $(\nabla n^{\gamma})/n$ $\qquad$ pressure nonlinearity

4. $n\overline{v}$ $\qquad$ current nonlinearity

5. $\overline{\nabla} n \overline{v}$ $\qquad$ continuity nonlinearity

The derivation of Eq. 2 is then set up so that the effect of each nonlinearity can be identified in the final answer.

Once the equations are entered, a functional Taylor series expansion is taken of the equations in the variables $\overline{v}(\overline{r}, t)$, $n(\overline{r}, t)$, $P(\overline{r}, t)$, $\overline{E}(\overline{r}, t)$, and $\overline{B}(\overline{r}, t)$ about an equilibrium which we take to be homogeneous (n_O, P_O, $\overline{B}_O$ constant and $\overline{v}_O \equiv 0$, $\overline{E}_O \equiv 0$). In practice $\overline{P}$ might be eliminated first to reduce the number of variables, but this is not necessary. For the fluid model, the only nonalgebraic nonlinearity occurs in the pressure term of the force equation, so it is sufficient just to expand this equation in $n(\overline{r}, t)$. The pressure term then to second order becomes

$$-\frac{\overline{\nabla} P}{n} = -\frac{P_O}{n_O^{\gamma}} \frac{\overline{\nabla} n^{\gamma}}{n} = -\frac{\gamma P_O}{n_O^2} \overline{\nabla}(n-n_O) - \frac{\gamma(\gamma-1)P_O}{2n_O^3} \overline{\nabla}(n-n_O)^2 + \frac{\gamma P_O}{n_O^3}(n-n_O)\overline{\nabla}(n-n_O).$$ (7)

If we let $P_O = n_O \kappa T$, then

$$-\frac{\overline{\nabla} P}{n} = -\gamma \kappa T \frac{\overline{\nabla} n}{n_O} - \gamma(\gamma-2) \kappa T \frac{(n-n_O)}{n_O} \frac{\overline{\nabla} n}{n_O}.$$ (8)

Next, each variable is expanded in a power series in an arbitrary parameter L which

might be the amplitude of the electric field.

$$\overline{v}(\overline{r}, t) = \overline{v}_O + L\overline{v}_1(\overline{r}, t) + L^2\overline{v}_2(\overline{r}, t) \ldots \tag{9}$$

$$n(\overline{r}, t) = n_O + Ln_1(\overline{r}, t) + L^2 n_2(\overline{r}, t) \ldots \tag{10}$$

etc.

The resulting equations are then ordered in powers of L and structured so that products of lower order terms are "driving" the higher order terms. These two steps of expanding and ordering are carried out by a single function that we have implemented, EXPEQS, which would then return

First-order equations:

$$m \frac{\partial v_1}{\partial t} = -\kappa T\gamma \frac{\overline{\nabla}n_1}{n_O} + q\overline{E}_1 + q\overline{v}_1 \times \overline{B}_O \tag{11}$$

$$\frac{\partial n_1}{\partial t} + n_O \overline{\nabla} \cdot \overline{v}_1 = 0 \tag{12}$$

$$\overline{\nabla} \times \overline{E}_1 = - \frac{\partial B_1}{\partial t} \tag{13}$$

$$\overline{J}_1 = n_O \overline{v}_1. \tag{14}$$

Second-order equations:

$$m \frac{\partial v_2}{\partial t} + \gamma\kappa T \frac{\overline{\nabla}n_2}{n_O} - q\overline{v}_2 \times \overline{B}_O = -m(\overline{v}_1 \cdot \overline{\nabla}) \overline{v}_1 - \gamma(\gamma-2) \frac{\kappa T n_1 \overline{\nabla}n_1}{n_O^2} + q\overline{v}_1 \times \overline{B}_1 \tag{15}$$

$$\frac{\partial n_2}{\partial t} + n_O \overline{\nabla} \cdot \overline{v}_2 = -n_1 \overline{\nabla}_1 \cdot \overline{v}_1 - (\overline{v}_1 \cdot \overline{\nabla})n_1 \tag{16}$$

$$\overline{J}_2 = n_O \overline{v}_2 + n_1 \overline{v}_1. \tag{17}$$

For three-wave coupling it is sufficient to carry this ordering to L^2, but for higher order interactions the procedure is continued to higher powers of L. This simply involves specifying to EXPEQS the highest power of L to be considered.

Now the equations are transformed by heuristic pattern rules such as $\frac{\partial}{\partial t} \rightarrow j\omega$, $\overline{\nabla} \rightarrow -j\overline{k}$. Second and higher order equations containing terms like $(\overline{v}_1 \cdot \overline{\nabla})\overline{v}_1$ are transformed to convolutions in ω and $\overline{k}$ space. If we assume that only a discrete set of first-order modes exists, then the convolutions are just summations. A single "transform function" has been implemented to take care of these continued operations. As an example, we show the result for the second-order force equation of mode n:

$$-i\omega^n m \bar{v}_2^{-n} + i\bar{k}^n \gamma \kappa T \frac{n_2^n}{n_o} - q\bar{v}_2^{-n} \times \bar{B}_o = \frac{1}{2} \sum_{a,b} - \left[im(\bar{v}_1^{-a} \cdot \bar{k}^b) \bar{v}_1^{-b} + im\left(\bar{v}_1^{-b} \cdot \bar{k}^a\right) \bar{v}_1^{-a} \right.$$

$$\left. + i\gamma(\gamma-2) \kappa T \frac{n_1^a n_1^b}{n_o^2} (\bar{k}^a + \bar{k}^b) - q\bar{v}_1^{-a} \times \frac{\bar{k}^b \times \bar{E}_1^{-b}}{\omega^b} - q\bar{v}_1^{-b} \times \frac{\bar{k}^a \times \bar{E}_1^{-a}}{\omega^a} \right], \qquad (18)$$

where $\omega^n = \omega^a + \omega^b$, $\bar{k}^n = \bar{k}^a + \bar{k}^b$, and $\bar{B}_1$ has been eliminated by use of Eq. 13.

The next step is to solve the first-order (linear) equations for $\bar{v}_1(\omega, \bar{k})$ in terms of $\bar{E}_1(\omega, \bar{k})$. This can be done by factoring the matrix operators relating all the variables, eliminating n_1, and then explicitly substituting vectors for $\bar{B}_o$, $\bar{v}_1$, and $\bar{E}_1$ and directly solving the vector equation. From this the linear conductivity can easily be found. At this point the linear dispersion relation can be derived directly. MACSYMA can then immediately evaluate this dispersion relation numerically for cases of interest or give ω-k plots for a given set of plasma parameters.

The second-order equations are solved by noting that the left-hand side operator is the same as that for the linear case (this is also true for higher order equations) which has already been obtained. Finding $\bar{J}_2$ is then a matter of solving for $\bar{v}_2$ by inverting the left-hand side operator of Eq. 18 and writing $n_1 \bar{v}_1$ in terms only of products of $\bar{E}_1$. The result for the fluid model, written in terms of the linear conductivity $\bar{\bar{\sigma}}$, is

Nonlinearity

$$\bar{J}_2^n = \frac{1}{n_o q} (\bar{E}^b \cdot \bar{\bar{\sigma}}^a \cdot \bar{E}^a)\bar{\bar{\sigma}}^n \cdot \frac{\bar{k}^b}{\omega^b} \qquad \qquad \text{Lorentz}$$

$$- \frac{1}{n_o q} \left(\frac{\bar{k}^b}{\omega^b} \cdot \bar{\bar{\sigma}}^a \cdot \bar{E}^a \right) \bar{\bar{\sigma}}^n \cdot \bar{E}^b \qquad \qquad \text{Lorentz}$$

$$- \frac{im}{n_o^2 q^3} (\bar{k}^b \cdot \bar{\bar{\sigma}}^a \cdot \bar{E}^a)\bar{\bar{\sigma}}^n \cdot (\bar{\bar{\sigma}}^b \cdot \bar{E}^b) \qquad \qquad \text{Convective}$$

$$+ \frac{1}{n_o q} \left(\frac{\bar{\bar{k}}^a}{\omega^a} \cdot \bar{\bar{\sigma}}^a \cdot \bar{E}^a \right) \bar{\bar{\sigma}}^b \cdot \bar{E}^b \qquad \qquad \text{Current}$$

$$- i \frac{\gamma \kappa T}{n_o^2 q^3} \left(\frac{\bar{k}^n}{\omega^n} \cdot \bar{\bar{\sigma}}^b \cdot \bar{E}^b \right)\left(\frac{\bar{k}^a}{\omega^a} \cdot \bar{\bar{\sigma}}^a \cdot \bar{E}^a \right) \bar{\bar{\sigma}}^n \cdot \bar{k}^n \qquad \qquad \text{Continuity}$$

$$- i \frac{\gamma(\gamma-2) \kappa T}{n_o^2 q^3} \left(\frac{\bar{k}^b}{\omega^b} \cdot \bar{\bar{\sigma}}^b \cdot \bar{E}^b \right)\left(\frac{\bar{k}^a}{\omega^a} \cdot \bar{\bar{\sigma}}^a \cdot \bar{E}^a \right) \bar{\bar{\sigma}}^n \cdot \bar{k}^b \qquad \qquad \text{Pressure}$$

$$+ (a \longleftrightarrow b). \qquad \qquad (19)$$

Note that the complete expression for $\overline{J}_2^n$ is summed over a and b, summed over species, and symmetrized with a and b replaced by b and a. The various nonlinearities have been distinguished so that they may be traced through independently.

In summary, once the equations are entered, the process of expanding, ordering, and transforming is automatic. The solution of the transformed equations can be done automatically, but greater efficiency in controlling the form of the answers is achieved by semiautomatic operation which directs MACSYMA in the sequence of steps (that is, which equations to solve first, which variables to eliminate at which point, etc.). The aim is to develop general techniques which can be used for a wide class of problems.

b. Evaluation of Nonlinear Coupling Coefficients

The evaluation of the coupling coefficient is defined in Eq. 2 and, by use of Eq. 19, consists in carrying out the matrix multiplications, substitution of values for the ω, $\overline{k}$, and $\overline{E}$, and structuring the result in an understandable form. Our objective is to gain physical understanding of the coupling by observing the effects of different nonlinearities and of various approximations (electrostatic, infinite or zero magnetic field, and so forth).

The possible sequences in which the evaluation steps can be carried out are indicated in Fig. XVI-22. Consider first the right branch MM_3. Here we first carry out the matrix multiplications for the most general case. These results are very large, but we can store them for later use, thereby saving the time required for these multiplications when each new case is considered. This method is good for getting quick answers but suffers because the details are not exhibited in the calculations. These details are some-times important for understanding why particular terms are zero, why the symmetrizing terms cause cancelation or which nonlinearity is dominant. Hence the center branch SC_2 is an important alternative. In this approach polarizations $\overline{k}$ and ω for a specific case of interest are substituted before the matrix multiplications are carried out. The tree also illustrates different ways in which approximations can be introduced. We can first make approximations in our model, such as electrostatics ($\overline{k}$ and $\overline{E}$ parallel), infi-nite magnetic field or zero magnetic field, by taking limits. This is indicated by the left branch A_1. By observing matrix multiplications at $MM_{1\ell}$, we can see what general effects this has before evaluating specific cases at $SC_{1\ell}$ or we can get more information on a specific case by evaluating it at SC_{1r} before the multiplications. Again, if we are interested in quick answers to a particular problem, we can make approximations at A_{3r} and store the results (which are the same as those for $MM_{1\ell}$) for ready evaluation.

Approximations can also be introduced after more general answers for specific cases have been calculated (A_2, $A_{3\ell}$). These answers should, of course, check with the results of making approximations at an earlier step. Correction terms can be derived directly by Taylor series expansion of the answers in the approximated parameters.
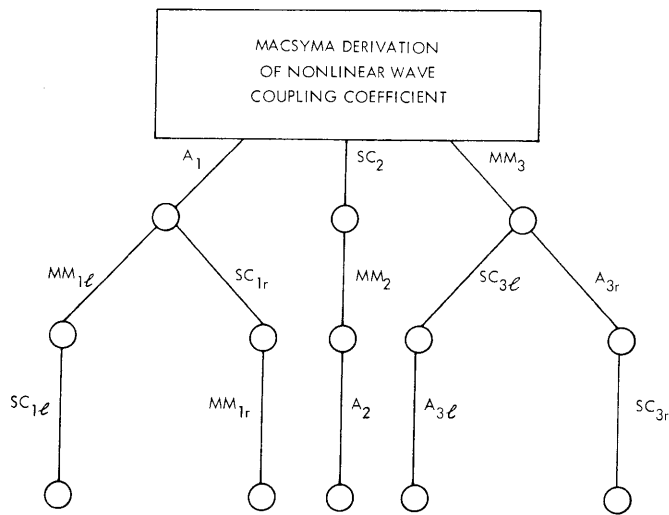
Fig. XVI-22.   Alternative ways of evaluating the nonlinear coupling of waves.
O: Results of operations indicated on branches.
A: Approximations (e. g., electrostatics, $B_o \rightarrow 0$ or ∞, Taylor series expansions).
SC: Substitute for parameters of a special case.
MM: Evaluate the matrix multiplications.

Approximations relating only to a given problem can be introduced by other expansions.

If numerical answers are desired, either for comparison of terms or for evaluation of coupling coefficients, numbers can be substituted and calculations performed directly on the resulting forms.   It is often useful to have a quasi-numerical evaluation by putting in numbers for all parameters but one, say, magnetic field, so that functional dependencies can be determined.   These and other numerical evaluations can be done at any step in the derivation and/or evaluation of the coupling coefficient.

We are now implementing the tree system of evaluation shown in Fig. XVI-22.

References

1. Proc. Second Symposium on Symbolic and Algebraic Manipulation, S. R. Petrick (Ed.) (Association for Computing Machinery — SIGSAM, New York, 1971).   The MACSYMA papers start on pp. 59, 78, 282, 305, 311, 427, and 458.

2. MACSYMA User's Manual, Project MAC, M. I. T., September 1971.

3. A. Bers, Les Houches Lectures in Plasma Physics — July 1972 (Gordon and Breach Publishers, New York, in press).

XVI. APPLIED PLASMA RESEARCH[*]

B. Plasma Physics and Engineering

Academic Research Staff

Prof. R. A. Blanken   Prof. E. P. Gyftopoulos
Prof. T. H. Dupree   Prof. L. M. Lidsky

Graduate Students

C. T. Breuer   D. L. Ehst   D. S. Komm
L. Bromberg   A. Hershcovitch   G. D. Pine
W. S. Chow   B. H. Hui   C. A. Primmerman
P. W. Chrisman, Jr.   J. H. Swailes

RESEARCH OBJECTIVES

1. Nonlinear and Turbulence Theory of Plasmas

We are pursuing a theoretical study of phase space density granulation in plasmas that contain strong magnetic fields. At large scale sizes perpendicular to the field, these granulations behave like eddies in a turbulent incompressible fluid and produce greatly enhanced particle transport across the field. For small scale sizes the granulations resemble clumps of plasma that are carried around in cyclotron orbits. The principal objective of this research is to understand the physics of the various processes involved and to develop useful analytical descriptions. At a later stage we plan to apply the theory to a number of practical problems, such as plasma confinement and cyclotron radiation.

T. H. Dupree

2. Nonlinear Saturation Experiments

Nonlinear theory predicts that the saturation level of various plasma instabilities is affected by the presence of nonresonant wave activity. We are testing these predictions in our low-density fully ionized plasma column. The column is subject to naturally occurring Kelvin-Helmholtz shear instabilities. We are measuring the effect of driven ion cyclotron waves on the saturation level of the shear waves.

G. D. Pine, L. M. Lidsky

3. Stabilized Mirror Experiment

The reconstruction of our magnetic mirror experiment has been completed, with the installation of a new vacuum chamber and a set of quadrupole Ioffe windings. Plasma experiments in the stabilized mirror will commence in a few weeks with the production of electron cyclotron resonance plasmas. Next year we plan to study in detail the properties of the hot electron plasmas produced and the time and spatial development of the velocity space instabilities which we expect to occur.

R. A. Blanken, G. D. Pine

---

4. Far Infrared Plasma Diagnostics

Our 337-μm HCN laser will be used in conjunction with the stabilized mirror experiment to study the time and spatial development of turbulence associated with velocity space instabilities. A study of the infrared synchrotron radiation for Alcator is also in progress. In this study we use a novel Fabry-Perot interferometer with millisecond time response.

R. A. Blanken, D. S. Komm

5. Study of Anomalous Resistivity

The highly ionized plasma column will be used to measure plasma resistivity in the regime in which the electron drift velocity is comparable to the ion acoustic velocity. We hope to eliminate the problem of unknown sheath voltage drops by using large-area emitting electrodes as current source and sink.

C. A. Primmerman, L. M. Lidsky

C.   Plasma Effects in Solids

Academic Research Staff

Prof. A. Bers

Graduate Students

J. H. Cafarella

RESEARCH OBJECTIVES AND SUMMARY OF RESEARCH

During the past year we have completed two major studies related to the interaction between acoustic surface waves on a piezoelectric and electrons at the surface of a semiconductor.

The first study was a theoretical analysis of the interaction in the presence of inhomogeneities in the electron density.[1] Such inhomogeneities are unavoidable for drifted electrons at the surface of semiconductors when the applied electric field is raised to the value required for maximum amplification of the acoustic surface wave. The analysis thus gives a possible explanation of the observed fact that one cannot reach the maximum gain predicted by a homogeneous theory.

In the second study we have demonstrated a new method for determining the mobility of electrons at the surface of semiconductors.[2] This method involves the measurement of the surface acoustoelectric current and has numerous advantages over the usual mobility measurements (see Section XVI-C. 1).

For the next year we plan to continue our study of direct electrical excitation of electron surface waves on a semiconductor.

A. Bers

References

1. B. E. Burke and A. Bers, Appl. Phys. Letters 21, 449-451 (1972).

2. J. H. Cafarella, A. Bers, and B. E. Burke, Proc. 1972 IEEE Ultrasonics Symposium, IEEE Publication No. 72 CHO 708-8 SU New York 1972, pp. 181-185.

1.   SURFACE MOBILITY ON SILICON FROM ACOUSTOELECTRIC
     CURRENT MEASUREMENTS

J. H. Cafarella, A. Bers

We have previously reported[1,2] the theory of the surface acoustoelectric current and proposed that it be used in measuring the mobility of carriers at semiconductor

surfaces. We now give the results of experiments using this method. It must be empha-
sized that this new method is radically different from other mobility measurement tech-
niques. Previous methods[3,4] relied upon a measurement of surface conductivity and
therefore only the product of mobility and mobile carrier density could be determined.
A separate measurement of the carrier density at the surface was therefore required.
Furthermore, in the presence of surface states, an additional experiment was needed
to determine the percentage of carriers that are mobile. The technique described here
yields the surface mobility in a single measurement and does not require a separate
determination of carrier concentration. Although the mobility measured in this way is
multiplied by a trap-dependent factor, we have shown[1] that this factor is unity, provided
that either the trap density is kept sufficiently low or the experiment is performed at
acoustic-wave frequencies much higher than the inverse time constants of the surface
states.

A qualitative understanding of the measurement can be obtained from Fig. XVI-23.
A surface elastic wave on a piezoelectric $(LiNbO_3)$ is shown, and adjacent to it is a high
resistivity n-type silicon crystal with a conducting sheet of electrons at its surface.
The periodic electric fields of the surface wave extend above the piezoelectric surface
and interact with the electrons. The entrainment of the electrons in the traveling poten-
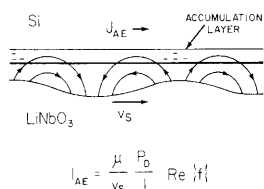tial wells established by the surface wave leads to a net flux of carriers in the direction

Fig. XVI-23.
Surface acoustoelectric current.

of the wave. If the ends of the silicon are shorted, a portion of the terminal current
flow is steady and is termed the surface acoustoelectric current I_{AE}. We have previ-
ously derived[1] an expression for I_{AE},

$$I_{AE} = \frac{\mu P_d}{v_s L} \text{Re} \{f\},$$ (1)

where μ is the carrier mobility, P_d is the power given up to the carriers by the surface
wave, v_s is the surface-wave velocity, L is the interaction length, and f is a trap-
dependent factor.[1]

We have performed experiments using low trap density silicon samples so that
$f_o \approx 1$, and hence $f \approx 1$ at all frequencies. Using Eq. 1 with Re $\{f\}$ = 1 and knowing v_s

and L, we need only measure P_d and I_{AE} to determine the mobility. The power given up by the wave to the silicon, P_d, may be found by measuring the input power to the delay line, P_o, and the excess delay line insertion loss attributable to the silicon, Δ; then $P_d = P_o[1 - \exp(.23\,\Delta)]$, where Δ is expressed in dB. For our experimental parameters $I_{AE} \sim 10^{-9}$ A for an input acoustic power $P_o \sim 10^{-6}$ W. Since the sample resistance was typically 1 MΩ, a Keithley electrometer (with input impedance $\sim 10^8$ MΩ) was used to measure both the open-circuit voltage and the sample resistance. This method of determining I_{AE} also avoids complications that may arise from bad contacts.

Fig. XVI-24 is a schematic diagram of the acoustoelectric current experiment. A silicon sample is placed, with its accumulated side down, on a LiNbO$_3$ delay line. Silicon dioxide rails on the delay line prevent mechanical contact in the acoustic channel. The LiNbO$_3$ lies on the field plate, a piece of conductively coated glass. A bias voltage applied between the silicon and the field plate controls the sheet electron density in the accumulation layer.
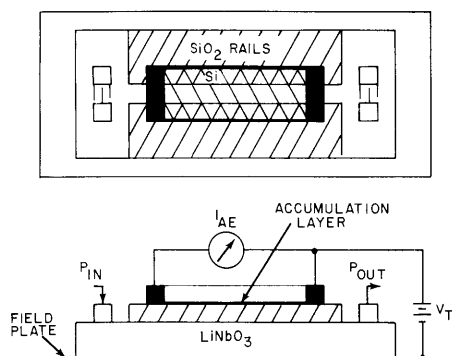

Fig. XVI-24.
Experimental configuration.

The properties of the LiNbO$_3$ delay line and Si sample are listed in Fig. XVI-25. The LiNbO$_3$ cut is the usual one, while the Si has much higher resistivity than is normally encountered in semiconductor work. In order that the surface-state density be low in these samples, particular attention has to be paid to the crystal orientation and the oxide preparation. The (100) direction for surface normal yields the lowest surface-state density in silicon of any orientation. Experience has also shown that the method used for oxide preparation yields an extremely low surface-state density.

Mobility measurements were made for electron surface densities from 1.5×10^{10} cm^{-2} to 5×10^{11} cm^{-2}. The acoustic-wave frequency

<u>LiNbO$_3$</u>

- Y-CUT Z-PROPAGATING
- v_s = 3485 m/s
- Cr-Au TRANSDUCERS (166 MHz-10 FINGER PAIRS)
- SPUTTER DEPOSITED SiO$_2$ RAILS (450Å THICK-20 mil CHANNEL)

<u>Si</u>

- 30 KΩ cm ($n_o \approx 10^{11}$/cm^3)
- n$^+$ CONTACTS (PHOSPHOROUS DOPED)
- THERMAL OXIDE GROWN IN DRY O$_2$ ANNEALED IN N$_2$ (PHOSPHOROUS GLASS GETTERED)
- (100) NORMAL   (110) CURRENT

Fig. XVI-25. Material properties.

was 166 MHz; the input power range was 3-30 μW. A sheet model for the accumulation layer, as assumed in the analysis, requires that the layer thickness be much less than an acoustic wavelength. At the lowest surface density, 1.5×10^{10} cm^{-2} corresponding to a surface potential of $8\kappa T/e$, the maximum sheet thickness was ~4 μ, which was 1/5 of the acoustic wavelength. The thickness becomes 1/10 of this acoustic wavelength at a surface potential of $8.8\kappa T/e$, and exponentially smaller at higher surface potentials.
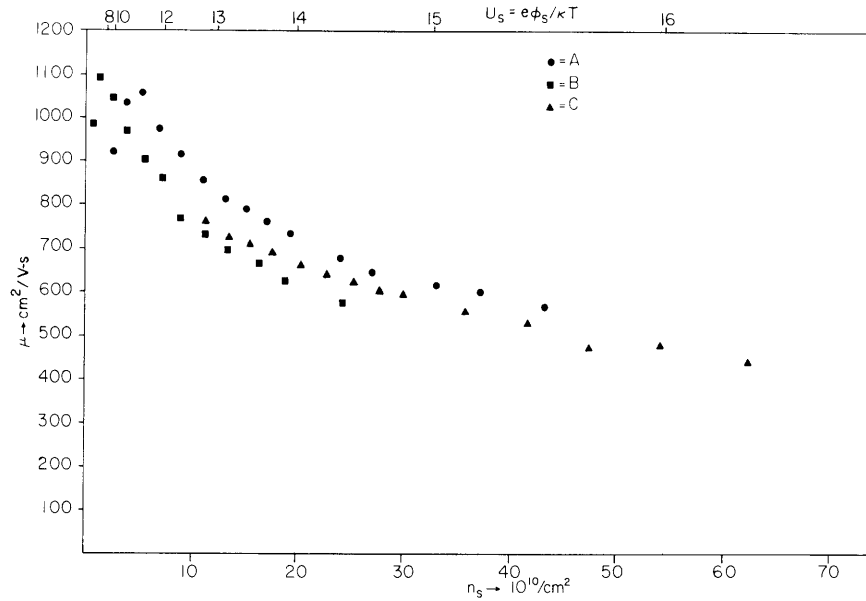
Fig. XVI-26. Mobility vs electron sheet density.

Figure XVI-26 shows mobility results for three samples tested. The mobilities range from 1100 cm^2/V-s for surface densities of 10^{10} cm^{-2}, to 450 cm^2/V-s at 5×10^{11} cm^{-2}. The mobility for low densities apparently approaches the bulk value. In this region of low densities, the spread in mobility is probably due to inhomogeneities in the electron sheet density which affect the acoustoelectric interaction.[5] The higher densities are formed by uniformly accumulating the surface with the applied transverse electric field, and there is a much narrower mobility spread.

To check the self-consistency of our measurements and assumptions, we have used the measured values of mobility and conductance to determine the carrier sheet density, and we have also determined this density from a measurement of the silicon-to-field-plate capacitance. These densities, $n_{s\mu}$ and n_{sc}, respectively, are plotted against each other for all samples in Fig. XVI-27. The fact that $n_{s\mu} = n_{sc}$ (within experimental error, and for the entire range of applied normal fields) shows that the effects of surface states were indeed negligible, and gives us confidence in the mobility determination
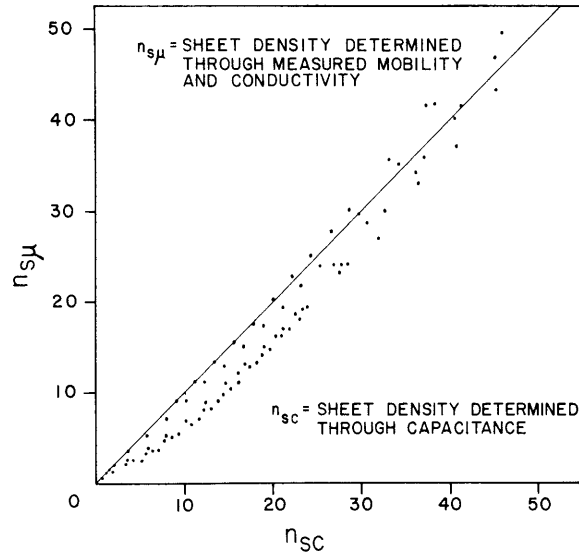
Fig. XVI-27.   Electron sheet density by two independent methods.

from the acoustoelectric current measurements.

In Fig. XVI-28 we compare the present experiment (shaded area) with those of others.   Fowler, Fang, and Hochberg[3] (Curve 3) used the Hall effect, while Leistiko,
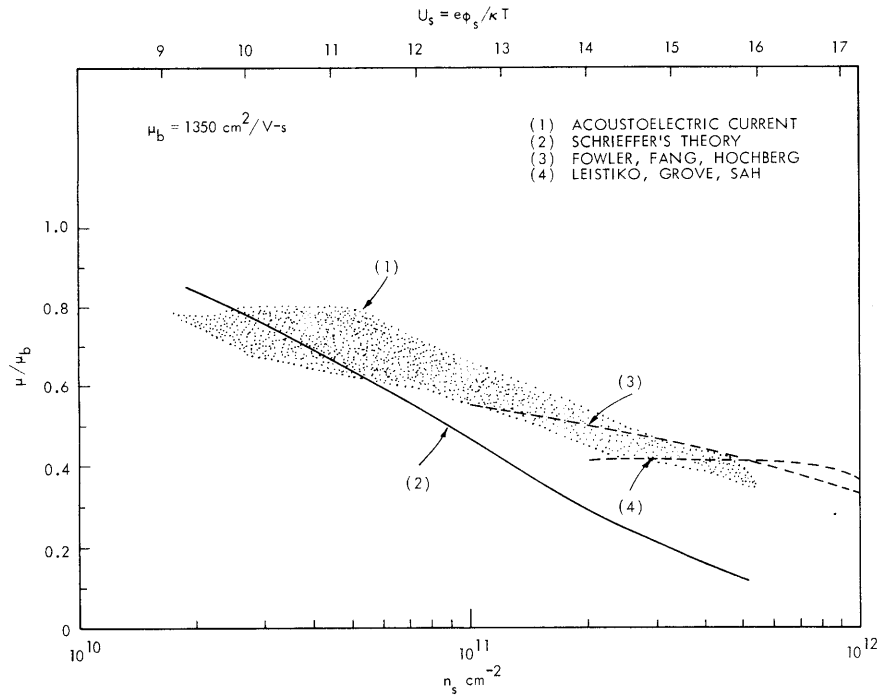

Fig. XVI-28.   Theoretical and measured mobilities.

Grove, and Sah[4] (Curve 4) used capacitance voltage measurements on a MOSFET to calculate the carrier density. Curve 2 furnishes a theory for surface mobility by Schrieffer,[6] who hypothesized that carriers experience diffuse scattering from the surface. In light of the experimental results yielding higher mobilities it would appear that carrier scattering from the surface is not entirely diffuse.

References

1. J. H. Cafarella and A. Bers, Quarterly Progress Report No. 104, Research Laboratory of Electronics, M.I.T., January 15, 1972, p. 217.

2. A. Bers, Quarterly Progress Report No. 105, Research Laboratory of Electronics, M.I.T., April 15, 1972, p. 112.

3. A. B. Fowler, F. Fang, and F. Hochberg, IBM J. Res. Develop. 8, 427 (1964).

4. O. Leistiko, Jr., A. S. Grove, and C. T. Sah, IEEE Trans., Vol. ED-12, No. 5, pp. 248-254, May 1965.

5. B. E. Burke and A. Bers, Appl. Phys. Letters 21, 449-451 (1972).

6. J. R. Schrieffer, Phys. Rev. 97, 641 (1955).

XVI. APPLIED PLASMA RESEARCH[*]

D. Laser-Plasma Interactions

Academic and Research Staff

Prof. E. V. George   Prof. H. A. Haus   J. J. McCarthy
Prof. A. Bers   Dr. P. A. Politzer   W. J. Mulligan
                          Dr. A. H. M. Ross

Graduate Students

Y. Manichaikul   D. Prosnitz   C. W. Werner
J. L. Miller   D. Wildman

RESEARCH OBJECTIVES AND SUMMARY OF RESEARCH

Our research objectives are divided basically into two programs. One involves the study and construction of both a short-pulse (approximately 1-10 nanosecond) and a long-pulse (several hundred nanosecond) atmospheric pressure CO_2 laser. We are also constructing a CO_2 laser amplifier initiated by a high-energy electron beam. This amplifier will be the final one for our pulsed laser experiments.

The other program is devoted to theoretical and experimental studies of plasma heating using this laser system. Initially we shall make studies of a laser-produced plasma in both solid and gaseous targets, and studies of the optical mixing of two lasers in a low-density target plasma.

E. V. George

1. OPTICAL FREQUENCY MIXING IN A PLASMA

D. Prosnitz

Linear plasma theory has been extremely successful in predicting plasma phenomena solely because the second-order (nonlinear) terms of the expansion of the equations of motion are much smaller than the linear terms and can usually be ignored. Consequently, if we wish to investigate nonlinear effects, a method of enhancing the second-order terms must be found. Most nonlinear effects are proportional to the square of the electric field; hence, large fields will greatly increase second-order phenomena. The intense coherent radiation produced by gas lasers provides the necessary field strength. In light of these matters, we have undertaken a study of laser-plasma interactions using a 10.6 μm CO_2 laser. Specifically, we wish to study the nonlinear wave-wave mixing predicted by several authors.[1-3] In the course of this study I have observed a laser-induced near-resonant Stark shift of the 4713 Å line in helium.

This report has three parts. In the first part the theory and feasibility of a frequency-mixing experiment using CO_2 lasers is treated; in the second, the high-frequency Stark effect as a means of observing electrostatic oscillations of a plasma is discussed; and in the third, our experimental arrangement and some preliminary results from measurements of a laser-induced Stark shift in helium are presented.

Theory and Feasibility of a Frequency-Mixing Experiment
Using CO_2 Lasers

If $\omega \gg \omega_p$, electromagnetic radiation of frequency ω will not interact strongly with a plasma characterized by a plasma frequency $\omega_p = \sqrt{ne^2/m\epsilon_o}$, where n is the charge density, e and m the electron charge and mass, and ϵ_o the permittivity of free space. Since most high peak power lasers operate at frequencies above 3×10^{13} Hz, we are constrained to plasmas of densities $10^{19}/cm^3$ and above. If, however, two transverse electromagnetic waves of frequencies ω_1 and ω_2 and wave vectors $\vec{k}_1$ and $\vec{k}_2$ are allowed to mix and produce a third wave at their difference frequency $\omega_3 = \omega_1 - \omega_2$, there may be appreciable energy transfer to the electrostatic modes of the plasma. This method would then provide a means of transferring laser energy to moderate and low-density plasmas, despite the fact that ω_1 and ω_2 may both be much greater than ω_p.

Weyl[2] has solved the cold-plasma equations for the second-order density perturbation induced by two such transverse electromagnetic waves when their difference frequency is a normal mode of the plasma. In particular, when $\omega_3^2 = \omega_p^2 + 3k_3^2 v_T^2$ he shows that

$$\frac{n_2}{n} = \frac{2v_{D1}v_{D2}\omega_1\omega_2}{c^2 \nu \omega_p} \cos\beta \, \sin^2\beta/2. \tag{1}$$

Here n_2 is the second-order density perturbation; $\vec{k}_3 = \vec{k}_1 - \vec{k}_2$ is the wave vector of the wave of frequency ω_3; $v_T^2 = k_B T/m$ is the thermal velocity of the electron, with k_B Boltzmann's constant and T the electron temperature of the plasma; $v_{D1} = eE_1/m\omega_1$ is the electron RF velocity, with E the electric field of the laser; ν is the damping rate (either the collisional electron neutral damping rate or Landau damping rate, whichever is greater); and β is the angle between the two incident electric fields. (See Fig. XVI-29.)

Now it is convenient to define a quantity $f = k_3 \lambda_D$, where $\lambda_D = v_T/\omega_p$ is the standard Debye length. Furthermore, we assume that $|k_1| \approx |k_2| = |k| = \frac{|k_3|}{2 \sin\beta/2}$. Then

$$\sin^2 \beta/2 = \frac{k_3^2}{4k^2} = \frac{1}{4}\left(\frac{f}{k\lambda_D}\right)^2$$

and substituting this in Eq. 1, we obtain

$$\frac{n_2}{n} = \frac{1}{2}\frac{v_{D1}v_{D2}}{v_T^2}\frac{\omega_p}{\nu}f^2. \tag{2}$$

In deriving Eq. 2 we used the fact that β is small and $\cos\beta \approx 1$.

Sjolund and Stenflo[3] examined this same problem using a coupled-mode approach and arrived at

$$\frac{n_2}{n} = \frac{1}{2}\frac{v_{D1}v_{D2}}{v_T^2}\frac{\omega_p}{\nu}f^2(1-e^{-\nu t}). \tag{3}$$

This is equivalent to Weyl's solution with $t \gg 1/\nu$. Sjolund and Stenflo assumed that the transverse modes are relatively unaffected by the growth of the longitudinal mode at frequency ω_3, and that f must be kept small in order to insure small Landau damping. If we assume a helium plasma with an electron temperature of 3 eV and a neutral gas pressure of 0.5 Torr, we find the electron neutral collisional damping rate to be $2\times10^9/s$.
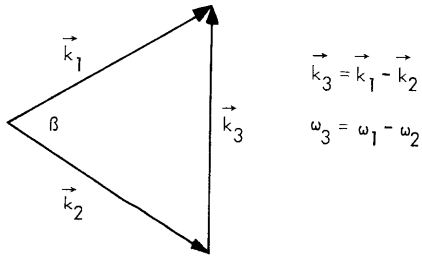

$$\vec{k}_3 = \vec{k}_1 - \vec{k}_2$$
$$\omega_3 = \omega_1 - \omega_2$$

Fig. XVI-29. Geometry of laser mixing.

Furthermore, if the plasma has a charge density of $1.2 \times 10^{14}/cm^3$, chosen so that $\omega_p/2\pi = 10^{11}$ Hz, the Landau damping will be equivalent to the collisional damping when $f = 0.25$. This determines β, the optimal angle for the interaction.

In order to form a rough estimate of the magnitude of the interaction, assume that $v_{D1} \approx v_{D2} = v_T/5$. This condition determines the amount of energy that must be supplied by the lasers. Thus

$$\frac{n_2}{n} = \frac{1}{2}\left(\frac{v_D}{v_T}\right)^2\frac{\omega_p}{\nu}f^2 = \frac{1}{2}\left(\frac{1}{5}\right)\left(\frac{2\pi\times10^{11}}{2\times10^9}\right)(0.25)^2 \cong 0.4.$$

The lasers induce a 40% density fluctuation, provided that saturation does not occur first. (Actually the perturbation method is not valid for n_2/n much greater than 0.1.) Also note that $1/\nu \approx 0.5 \times 10^{-9}$ s, which insures that this value of n_2/n is reached in a very short time (see Eq. 3). We must now determine what kind of laser will excite this density perturbation. The laser must meet two essential requirements: The frequency of the laser must be tunable so that we may set $\omega_3 = \omega_1 - \omega_2 \approx \omega_p$, and the laser must have sufficient power to provide an RF velocity of one-fifth the thermal velocity.

The carbon dioxide laser emits intense coherent radiation at several different frequencies. Adjacent rotational laser lines are separated ~55×10^9 Hz. Two such lasers tuned, by means of a blazed diffraction grating, to a difference frequency of ~110×10^9 Hz would then meet the first condition (for a charge density of $1.2 \times 10^{14}/cm^3$).

A 3 eV electron has a thermal velocity v_T of 7.3×10^7 cm/s. We then need an RF drift velocity of 1.5×10^7 cm/s to meet the second condition. If we use 10.6 μm radiation, an electric field strength of 1.5×10^6 V/cm is necessary. A laser producing a peak power of 2×10^6 W focused to a spot of radius 100 μm would have such an electric field. As carbon dioxide lasers deliver 0.2 J in 100 ns, we see that the second condition is also met.

We have not considered the effect of plasma inhomogeneities, but Rosenbluth and Liu[4] have shown that this does not greatly affect the calculations presented here. Two properly tuned CO_2 lasers should mix in a helium discharge of moderate density to produce substantial second-order electrostatic oscillations.

High-Frequency Stark Effect as a Means of Observing
Electrostatic Oscillations of a Plasma

We shall now discuss the detection of the second-order density perturbation. We have demonstrated that two laser beams focused to a spot size of 100 μm and having a 100-ns halfwidth would provide field strengths sufficient to induce the interaction. The diagnostic apparatus must thus be capable of probing a volume of 10^{-6} cm^3 with good time resolution. Spectroscopic diagnostics meets this requirement.

The density perturbations induce electric field fluctuations in the plasma which in turn cause Stark shifts of the helium emission lines. These shifts will indicate the presence of the density fluctuations and allow a determination of the fluctuation frequency and magnitude. A brief examination of the ac Stark shift[5-7] will show exactly how this is done.

For the sake of simplicity, we assume a three-level atom (Fig. XVI-30). Transitions from levels A to B and from levels B to C are allowed, while an A to C transition is forbidden by dipole selection rules. Levels A and B are relatively close together, but level C is far from both A and B. The Hamiltonian of the

atom in the presence of an electromagnetic field may be written

$$H = \frac{p^2}{2m} - \frac{e}{mc} \vec{P} \cdot \vec{A} + \frac{e^2}{2mc^2} A^2 = H_o + H^1, \tag{4}$$

where P is the electron conjugate momentum, A is the electromagnetic vector potential, $H_o = p^2/2m$ is the unperturbed Hamiltonian, and $H^1 = -\frac{e\vec{P} \cdot \vec{A}}{mc} + \frac{e^2 A^2}{2mc^2}$ is the perturbation
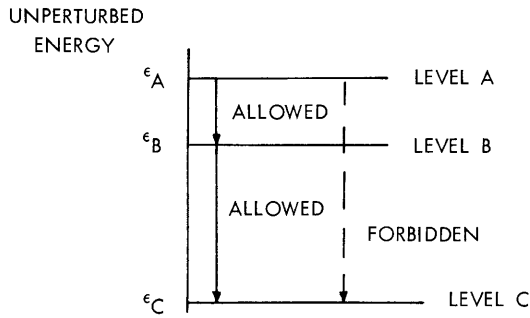

Fig. XVI-30. Three-level atom model.

Hamiltonian. If the electric field is not a radiation field but instead is produced by longitudinal plasma oscillations, H_o is unchanged and $H^1 = e\vec{E} \cdot \vec{r}$, where r is the electron's position vector. Furthermore, if ϵ_n and $|\phi_n\rangle$ are the unperturbed nondegenerate energy eigenvalues and eigenstates of the atom, we may write

$$H_o |\phi_n\rangle = \epsilon_n |\phi_n\rangle. \tag{5}$$

In a similar manner if E_n and $|\psi_n\rangle$ are defined as the perturbed eigenvalues and eigenstates,

$$H |\psi_n\rangle = E_n |\psi_n\rangle. \tag{6}$$

It is now convenient to assume that only levels A and B are "close" enough to interact. (The implications and validity of this assumption will be discussed.) $|\psi_n\rangle$ is now a linear combination of $|\phi_A\rangle$ and $|\phi_B\rangle$; that is, $|\psi_n\rangle = a_n |\phi_A\rangle + b_n |\phi_B\rangle$. We find a_n and b_n by substituting this expression for $|\psi_n\rangle$ in the Schrödinger equation (6). We then find[5]

$$\frac{a_n}{b_n} = \frac{H_{AB}}{E_n - H_{AA}}, \tag{7}$$

where E_n is the solution of

$$\begin{vmatrix} H_{AA} - E_n & H_{AB} \\ H_{BA} & H_{BB} - E_n \end{vmatrix} = 0$$

$$H_{nm} \equiv \langle \phi_n | H | \phi_m \rangle$$

and

$$E_n = \frac{H_{AA} + H_{BB} \pm \left((H_{AA} - H_{BB})^2 + 4H_{AB}^2 \right)^{1/2}}{2}. \tag{8}$$

$| \psi_n \rangle$ may be written in a convenient form by defining the quantity $\tan \gamma = \dfrac{2H_{AB}}{H_{AA} - H_{BB}}$ (see Davydov[5]). Using this simplification and substituting the (Eq. 8) value for E_n in Eq. 7, we find

$$| \psi_+ \rangle = \cos \gamma/2 \, | \phi_A \rangle + \sin \gamma/2 \, | \phi_B \rangle \tag{9}$$

$$| \psi_- \rangle = \sin \gamma/2 \, | \phi_A \rangle - \cos \gamma/2 \, | \phi_B \rangle. \tag{10}$$

Here $| \psi_\pm \rangle$ refers to $\pm$ in the solution for E_n (Eq. 8). Before proceeding to an ac field let us examine the case of a dc electric field applied to our atom. For this situation H'_{AB} may be written as $eE \langle \phi_A | z | \phi_B \rangle$, where z is the direction of the electric field. If H' is to be a true perturbation, $\tan \gamma$ must be small. We may then expand the square root in Eq. 8 to obtain

$$E_+ = H_{AA} + \frac{|H_{AB}|^2}{H_{AA} - H_{BB}} \tag{11}$$

$$E_- = H_{BB} - \frac{|H_{AB}|^2}{H_{AA} - H_{BB}}. \tag{12}$$

In Eqs. 11 and 12, $H_{AA} = \epsilon_A$ and $H_{BB} = \epsilon_B$ by virtue of the fact that the perturbation matrix element vanishes between identical states. H_{AB} is now equal to $eE \langle \phi_A | z | \phi_B \rangle$. The shifted energy levels and mixed eigenfunctions are shown in Fig. XVI-31.

Levels A and B show the standard Stark "level repulsion." We may also calculate the ratio of the allowed to forbidden lines in the presence of an electric field. This is seen to be $\cot^2 \gamma/2$. This ratio is convenient for calculating the electron
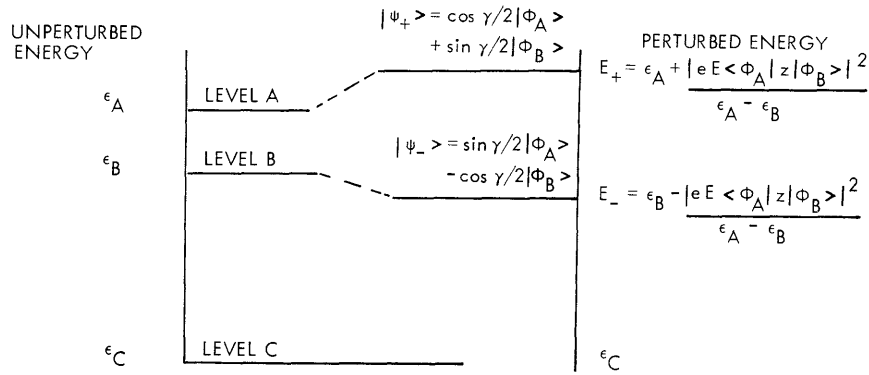
UNPERTURBED ENERGY

$|\psi_+> = \cos\gamma/2 |\Phi_A>$
$+ \sin\gamma/2 |\Phi_B>$

PERTURBED ENERGY

$E_+ = \epsilon_A + \dfrac{|eE<\Phi_A|z|\Phi_B>|^2}{\epsilon_A - \epsilon_B}$

ϵ_A LEVEL A

ϵ_B LEVEL B

$|\psi_-> = \sin\gamma/2 |\Phi_A>$
$- \cos\gamma/2 |\Phi_B>$

$E_- = \epsilon_B - \dfrac{|eE<\Phi_A|z|\Phi_B>|^2}{\epsilon_A - \epsilon_B}$

ϵ_C LEVEL C

ϵ_C

Fig. XVI-31. D-C Stark splitting of levels A and B.

densities in plasmas because it is proportional to the electric field in the plasma.

If the electric field is oscillating at a frequency ω, the situation is slightly different. The unperturbed energy levels now include the energy of the electromagnetic field $n\hbar\omega$, where n is the number of photons or longitudinal plasmons, and $\hbar$ is Planck's constant. The perturbation terms in the Hamiltonian allow the creation and annihilation of photons. The virtual states thus created are labeled levels A' and B' (see Fig. XVI-32). The states are virtual because they do not conserve energy. These virtual states

ENERGY
$\epsilon_A + n\hbar\omega$

LEVEL A

$\epsilon_B + (n+1)\hbar\omega$

LEVEL A'

$\epsilon_A + (n-1)\hbar\omega + \dfrac{H_{12}^2}{\epsilon_A - \epsilon_B - \hbar\omega}$

$\epsilon_A + (n-1)\hbar\omega$

LEVEL B'

$\epsilon_B + n\hbar\omega$

LEVEL B

$\epsilon_B + n\hbar\omega - \dfrac{H_{12}^2}{\epsilon_A - \epsilon_B - \hbar\omega}$

SATELLITE
ω_{+c}

STARK-SHIFTED
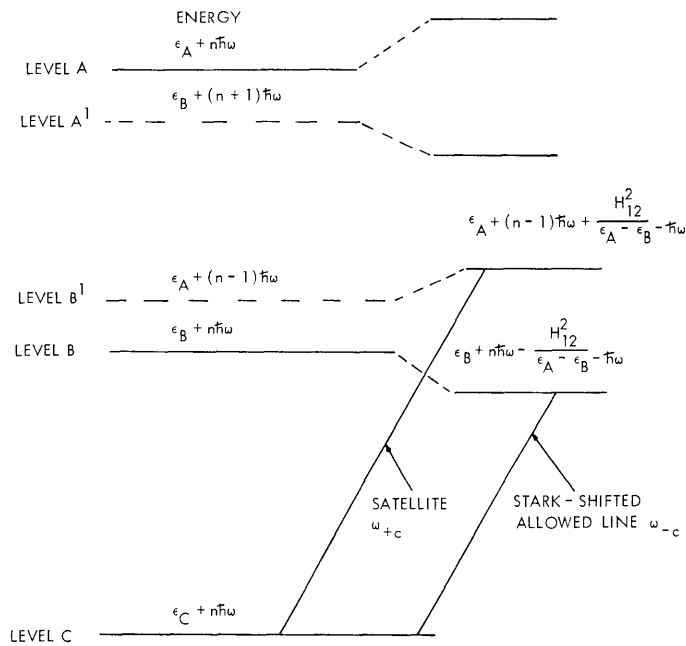ALLOWED LINE ω_{-c}

$\epsilon_C + n\hbar\omega$

LEVEL C

Fig. XVI-32. A-C Stark shift of nearly resonant atomic
levels A and B.

may mix with the unperturbed states to produce a Stark shift. Following the same pro-cedure that was used to calculate the dc Stark shift, and recognizing that H_{nn} now includes the electromagnetic field energy, we can calculate the energy shifts of levels B and B' (or A and A'). Using the same notation, we find

$$E_- = \epsilon_B + n\hbar\omega - \frac{H^2_{AB}}{\epsilon_A - \epsilon_B - \hbar\omega} \tag{13}$$

$$E_+ = \epsilon_A + (n-1)\hbar\omega + \frac{H^2_{AB}}{\epsilon_A - \epsilon_B - \hbar\omega}$$

$$|\psi_-\rangle = \cos \gamma/2 \ |\phi_B\rangle + \sin \gamma/2 \ |\phi_A\rangle$$

$$|\psi_+\rangle = \sin \gamma/2 \ |\phi_B\rangle - \cos \gamma/2 \ |\phi_A\rangle \tag{14}$$

$$\tan \gamma = 2H_{AB}/(\epsilon_A - \epsilon_B - \hbar\omega).$$

$|H_{ab}|^2$, found by quantizing the electric field in the standard manner,[8] is equal to

$$\frac{e^2 E^2}{2} \langle \phi_A | \vec{\epsilon} \cdot \vec{r} | \phi_B \rangle \langle \phi_B | \vec{\epsilon} \cdot \vec{r} | \phi_A \rangle,$$

where $\vec{\epsilon}$ is the polarization of the electromagnetic wave (in the direction of the electric field if plasmons are considered). Let us now consider transitions with frequencies

$$\omega_{-c} = \left(\epsilon_B - \epsilon_C - \frac{H^2_{AB}}{\epsilon_A - \epsilon_B - \hbar\omega} \right) \hbar^{-1}$$

$$\omega_{+c} = \left(\epsilon_A - \epsilon_C + \frac{H^2_{AB}}{\epsilon_A - \epsilon_B - \hbar\omega} - \hbar\omega \right) \hbar^{-1}.$$

The transition frequency ω_{-c} is just the Stark-shifted allowed line. The only dif-ference between the shift of this line in the ac and dc cases is in the modification of the denominator of the actual shift by the addition of the term $-\hbar\omega$. The transition at frequency ω_{+c} is, however, something new. This frequency is shifted from the for bidden line by $\hbar\omega$. It is one of the satellites first postulated by Baranger and Mozer.[8] (The other satellite can be found by considering the mixing of a virtual state of energy $\epsilon_A + (n+1)\hbar\omega$ and the state of energy $\epsilon_B + n\hbar\omega$.)

The ratio of the satellite intensity to allowed line intensity is $\tan^2 \gamma$

$$\left(\tan \gamma = \frac{2H_{AB}}{\epsilon_A - \epsilon_B - \hbar\omega}\right). \text{ If } \gamma/2 \text{ is small, we may write this ratio as}$$

$$\tan^2 \gamma/2 \approx \frac{e^2E^2}{2} \left\{\frac{|\langle\phi_A|\vec{\epsilon}\cdot\vec{r}|\phi_B\rangle|}{\epsilon_A - \epsilon_B - \hbar\omega}\right\}^2.$$

Following Baranger and Mozer, we assume random polarization of the electric field. (This is not strictly correct for laser electric fields or coherently generated plasma oscillations.) Then

$$\tan^2 \gamma/2 \approx \frac{e^2E^2}{6} \left\{\frac{|\langle\phi_A|\vec{\epsilon}\cdot\vec{r}|\phi_B\rangle|}{\epsilon_A - \epsilon_B - \hbar\omega}\right\}^2.$$

Now define

$$R_{AB} \equiv \frac{|\langle\phi_A|r|\phi_B\rangle|^2}{a_o^2}$$

$$a_o = \hbar^2/me^2.$$

Then finally

$$\tan^2 \gamma/2 = \frac{E^2e^2a_o^2R_{AB}}{6} \frac{1}{(\epsilon_A - \epsilon_B - \hbar\omega)^2}. \tag{15}$$

This, in fact, is Baranger and Mozer's result.

Before calculating some typical shifts, we must examine the validity of the assumption that only two levels (either A and B or B and B') are close enough to interact. Standard quantum-mechanical perturbation theory[9] shows that the perturbed energy level E_n is

$$E_n = \epsilon_n + \langle\phi_n|H'|\phi_n\rangle + \sum_{m\neq n} \frac{\langle\phi_n|H'|\phi_m\rangle\langle\phi_m|H'|\phi_n\rangle}{\epsilon_n - \epsilon_m}.$$

The term H'_{nn} vanishes as before, and the states $|\phi_n\rangle$ are nondegenerate. If, for one particular set of levels, $\epsilon_n - \epsilon_m - \hbar\omega$ is very small, the corresponding term in the sum, called a resonant term, will be very much larger than all other terms. We may then replace the entire sum by the one resonant term to obtain

$$E_n = \epsilon_n + \frac{H_{nm}^2}{\epsilon_n - \epsilon_m - \hbar\omega}$$

identical to Eq. 13 (ϵ_n contains the electromagnetic field energy $n\hbar\omega$).

The close-level assumption is equivalent to the assumption that $\epsilon_n - \epsilon_m - \hbar\omega$ is small for only one set of levels. For low frequencies ($\hbar\omega \ll \epsilon_n - \epsilon_m$) the two levels must have nearly the same energy. For higher frequencies two (and only two) levels are separated by $\sim\hbar\omega$.

In these computations we have ignored shifts caused by the magnetic component of the electromagnetic field. Mizushima[10] has shown that this shift is of precisely the same form as the electric shift.

$$\Delta\epsilon_{magnetic} = \frac{B_o^2}{2} \frac{|\langle \phi_n | \vec{\epsilon} \cdot \vec{M} | \phi_m \rangle|^2}{\epsilon_n - \epsilon_m - \hbar\omega},$$

where B_o is the magnetic field, and M the dipole moment of the atom ($M = e/2\mu(\vec{L}+2\vec{S})$, where μ is the magnetic permeability, $\vec{L}$ the orbital momentum quantum number, and $\vec{S}$ the spin quantum number). For the particular lines that we wish to study, this is a small correction to the total energy shift, but it will cause a slight splitting of atomic levels with different magnetic quantum numbers. With the proper choice of resonant levels, however, this could become a large shift. We intend to investigate this possibility further.

We plan to detect the electrostatic oscillations caused by the perturbations discussed in this report by observing the satellites of an allowed forbidden pair of lines in helium. (The satellite is at frequency ω_{+c} as discussed above.) The $4\,^1D, 2\,^1P$ and $4\,^1F, 2\,^1P$ transitions at 4922 Å is a suitable choice. The $2\,^1P$ level corresponds to level C in the model discussed in this report. Levels $4\,^1F$ and $4\,^1D$ correspond to levels A and B, respectively. The electric field oscillates at frequency ω_p which is much less than $\omega_1 - \omega_2$. The $4\,^1F$ and $4\,^1D$ levels are separated by 8×10^{-4} eV.

In order to calculate the ratio of the satellite intensity to the allowed line intensity (Eq. 15) the electric field strength must be computed. Using Poisson's equation $\vec{\nabla} \cdot \vec{E} = ne/\epsilon_o$, we find $\vec{k}_3 \cdot \vec{E} = n_2 e/\epsilon_o$. Now from our previous results, E is found to be

$$E = \frac{(0.4)ne\lambda_D}{f\epsilon_o} = 4 \times 10^4 \text{ V/cm.}$$

R_{AB} for the levels in question is 151.[8] Substituting the values of R_{AB} and E in Eq. 15 yields

$$\tan^2 \gamma/2 = 0.18$$

or an allowed line intensity to forbidden line intensity ratio of 5:1. If n_2/n_o should saturate at 10% instead of at 40% (as a result of competing processes which were not considered) the ratio becomes 80:1. This is still large enough to be seen. The satellite should provide a reasonable means of detecting laser-induced electrostatic oscillations. As we have mentioned, Eq. 15 is not absolutely correct if the electrostatic oscillations are coherently generated. Cooper et al.[11] have shown that the satellites are slightly polarized. The intensity is thus a function of the angle of observation. The maximum (minimum) signal is computed by replacing the factor of 1/6 in Eq. 15 by 7/40 (6/40). We introduce at most a 10% error by assuming random polarization.

A single laser may also induce satellites. If two levels can be found which are separated by approximately $\hbar\omega$, the satellite may be large enough to be observed. For the CO_2 laser, $\hbar\omega$ for one rotational transition is ~943 cm^{-1}. The 4 ^{3}S and 4 ^{3}P levels in helium are separated 919 cm^{-1}. These two levels have an R_{AB} of 1300 (see Wiese et al.[12]). The allowed line is at 4713 Å (4^{3}S-2^{3}P). The laser that we are using at present has a peak electric field of 10^4 V/cm. Focusing may increase this field substantially. Using Eq. 15 once again, we find

$$\tan^2 \gamma/2 = 0.06$$

or approximately one-third the previous answer. Focusing the laser will enhance the satellite intensity. We intend to take measurements on this satellite, as well as on the satellite induced by the laser mixing.

The Stark shift of the 4 ^{3}S level in the presence of laser radiation is given by Eq. 13. The satellite energy is given by Eq. 14 (see Fig. XVI-32). Note that $E_A - E_B - \hbar\omega$ is negative. This implies that the energy of the perturbed state is slightly above that of the unperturbed state. The calculated shift of the 4713 Å helium line in the presence of an E field of 10^4 V/cm is 0.06 Å. (Note that the 2 ^{3}P state is not resonant with any other helium line and does not shift significantly.) We have measured this shift and the results will be presented.

Experimental Arrangement and Preliminary Results

The apparatus used to measure the Stark shift includes a TEA CO_2 laser, a helium discharge tube, a 0.5 m Jarrell Ash spectrometer and a synchronous detection system (Fig. XVI-33). The TEA laser has been described elsewhere.[13] The radius of the helium discharge tube is 0.5 mm and its length is approximately 15 cm. At present, it runs on 5 Torr of helium. The discharge itself is a 25-μs voltage pulse which drives approximately 3.5 A through the tube.

The plasma discharge is run at 30 Hz. The laser is fired 15 times per second into the discharge. This arrangement allows synchronous detection of any laser-induced
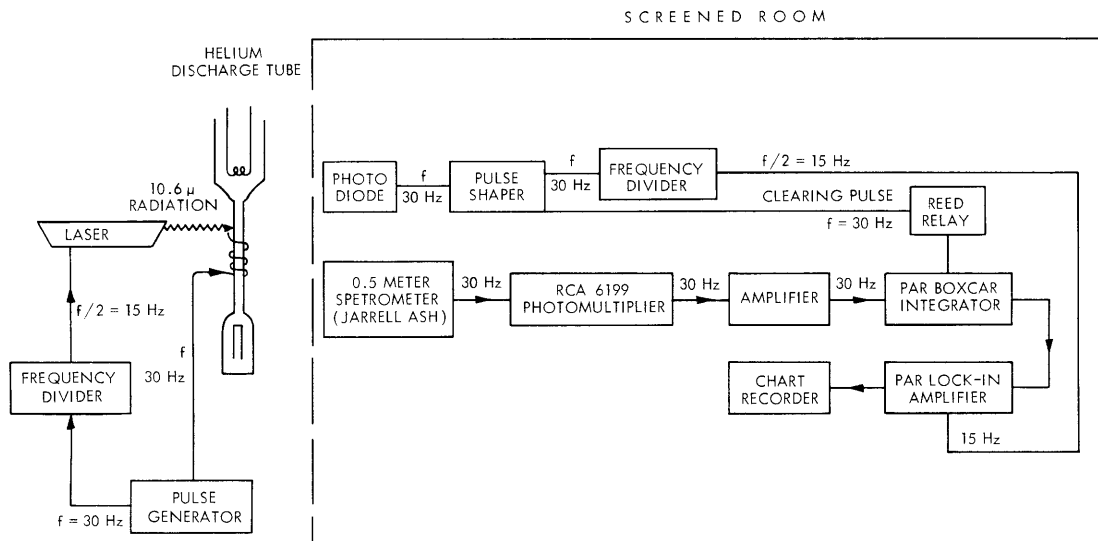
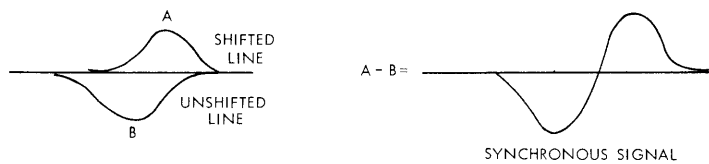Fig. XVI-33. Experimental apparatus for measuring the laser-induced Stark shift.

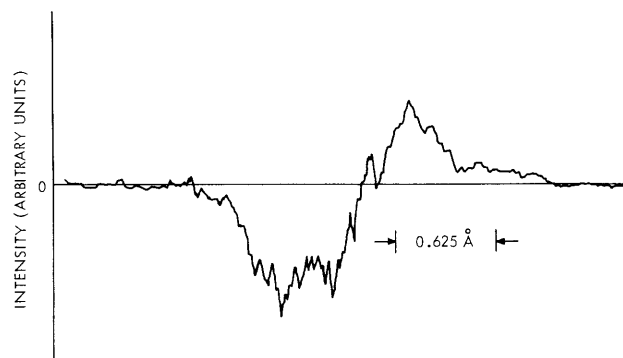Fig. XVI-34. Synchronous detection of laser-induced Stark shift.

Fig. XVI-35. Strip chart output showing synchronous detection of laser-induced Stark shift of the He I 4713 Å line.
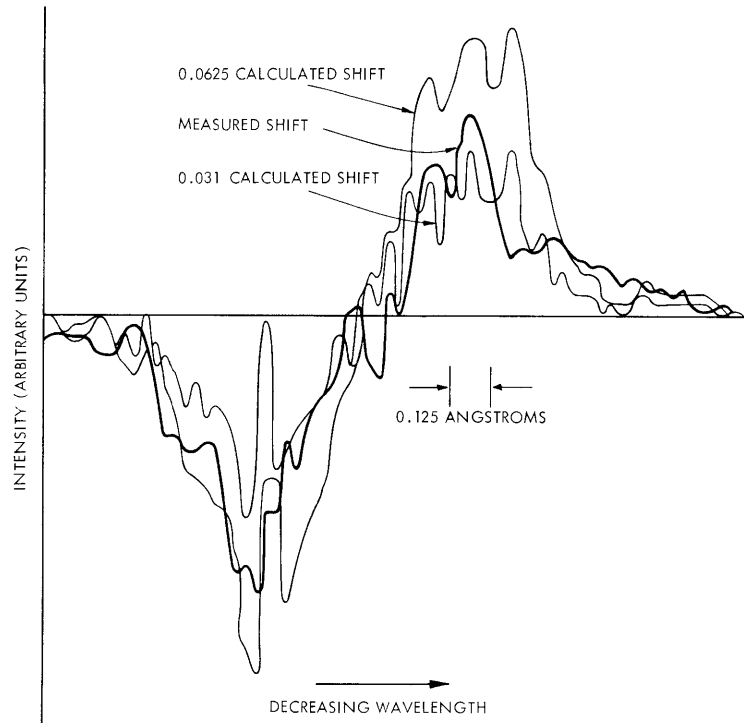
Fig. XVI-36.   Comparison of calculated Stark shift and measured Stark shift.

charge of the helium emission line.

The light signal from the plasma is routed through the spectrometer and onto an RCA 6199 photomultiplier. This signal is then amplified and passed to a gated boxcar amplifier (PAR 160). The boxcar is cleared after each pulse (30 Hz) so that the unit is actually functioning as a pulse stretcher. It only integrates a single pulse.

The output of the boxcar is fed to a PAR Model HR8 lock-in amplifier in conjunction with a 15-Hz reference signal obtained from a photodiode and a frequency divider. The final signal is displayed on a strip chart recorder. The spectrometer scans at 0.125 Å/min and the integration time of the lock-in amplifier is 20 s. All of the signal-processing equipment is located in a screened room to minimize the electrical noise generated by the laser firing circuit.

Figure XVI-34 shows the signal that would be expected if the laser shifts the $4\,^3S$ level. Figure XVI-35 is a typical signal produced on the chart recorder. Figure XVI-36 shows the predicted signals for a Stark shift of 0.0625 Å and of 0.031 Å. These curves were obtained by measuring the line shape at 4713 Å and then doing a point-by-point subtraction for each shift (as illustrated by Fig. XVI-34). This procedure automatically includes the instrument function in the calculation of the expected signal. (The points were 0.031 Å apart.) Also shown in Fig. XVI-36 is the

result of measurement of the Stark shift for an incident E field of 10^4 V/cm. The agreement with the predicted shift (0.06 Å) is quite good.

References

1. N. M. Kroll, A. Ron, and N. Rostoker, Phys. Rev. Letters 13, 83 (1964).

2. G. Weyl, Phys. Fluids 13, 1802 (1970).

3. A. Sjolund and L. Stenflo, "Parametric Coupling between Transverse Electromagnetic and Longitudinal Electron Waves," Physica 35, 499-505 (1967).

4. M. N. Rosenbluth and C. S. Liu, Phys. Rev. Letters 29, 701-705 (1972).

5. A. A. Davydov, Quantum Mechanics, translated from the Russian edition (Fitzmatgiz, Moscow, 1963) by Irene V. Schensted (Neo Press, Ann Arbor, Mich., 1966).

6. A. M. Bonch-Breuvich and V. A. Khodovoy, Sov. Phys. -- Usp. 93, 71-110 (1967).

7. S. H. Autler and C. H. Townes, Phys. Rev. 100, 703-722 (1955).

8. M. Baranger and B. Mozer, Phys. Rev. 123, 25-28 (1961).

9. P. A. M. Dirac, Principles of Quantum Mechanics (Oxford University Press, London, 1947).

10. M. Mizushima, Phys. Rev. 133, A414-A418 (1964).

11. W. S. Cooper and H. Ringler, Phys. Rev. 109, 179-236 (1969).

12. M. L. Wiese, M. W. Smith, and B. M. Glennon, "Atomic Transition Probabilities H through Ne," National Bureau of Standards Research Data Series, Natl. Bur. Stand. (U.S.) 4, Vol. 1, May 1966.

13. E. V. George, G. Bekefi, and B. Ya'akobi, Phys. Fluids 14, 2708-2713 (1971).

2. PLASMA DISPERSION FUNCTION: APPLICATION TO LAMB DIP

A. H. M. Ross

The complex plasma dispersion function,[1] defined as the integral

$$Z(\zeta) = \pi^{-1/2} \int_{-\infty}^{+\infty} dt \, \exp(-t^2)/(t-\zeta)$$

for Im $(\zeta) > 0$ and as the analytic continuation of this for Im $(\zeta) < 0$, is well known in plasma theory. It also finds application in the theory of optical properties of gases, when superposition integrals of Lorentzian resonances with Maxwellian-distributed center frequencies must be calculated. Although it has been recognized that these line-shape functions can be written in terms of tabulated functions,[2,3] they have not been
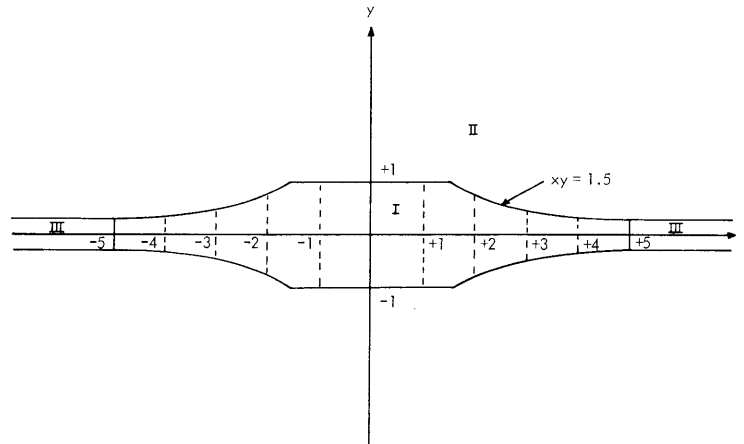
Fig. XVI-37. Partitioning of the complex ζ-plane.

used very much in numerical work. We have devised an improved algorithm for calculation of the plasma dispersion function anywhere in the complex ζ-plane, which should facilitate such analyses. Particular attention has been given to the region near the real axis, since some expansions are unsatisfactory there. An exact expression for the Lamb dip tuning curve of a gas laser based on the model of Freed and Haus[4] is given as an example of the use of $Z(\zeta)$ in optical physics.

$Z(\zeta)$ may be calculated by making expansions; we have found empirically that the following methods, with the partitioning of the complex ζ-plane shown in Fig. XVI-37, give reasonable efficiency and accuracy.

<u>Region I.</u> $|x| < 5$, $|y| < 1$, $|xy| < 1.5$

A Maclaurin series in $\zeta - \zeta_0$ is used, with ζ_0 a real integer such that the expansion is in the direction of increasing magnitude of the real part of ζ.

$$Z(\zeta) = \exp\left(\zeta_0^2 - \zeta^2\right)\left\{Z(\zeta_0) - 2(\zeta - \zeta_0) - 2\sum_{n=1}^{N}\left[C_{2n-1} + C_{2n}\frac{(\zeta - \zeta_0)}{2n+1}\right]\frac{(\zeta - \zeta_0)^{2n}}{(2n)!}\right\}$$

$$C_{k+1}(\zeta_0) = 2\left[\zeta_0 C_k(\zeta_0) + kC_{k-1}(\zeta_0)\right]$$

$$C_0 = 1$$

ζ_0 = integer part of x. That is,

$$0 \leq |x| < 1: \quad \zeta_O = 0$$

$$1 \leq x < 2: \quad \zeta_O = 1$$

$$2 \leq x < 3: \quad \zeta_O = 2$$

$$3 \leq x < 4: \quad \zeta_O = 3$$

$$\vdots$$

$$-2 < x \leq -1: \quad \zeta_O = -1$$

etc.

Convergence of this series when expanded in the direction of decreasing $|Re(\zeta)|$ is poor. Along the real axis the reason is clear; the consecutive terms alternate in sign. $\zeta_O = 0$ corresponds to the series used by Barberio-Corsetti.[5]

Region II. $|y| \geq 1$ or $|xy| \geq 1.5$

The continued-fraction expansion based on the asymptotic expansion of $Z(\zeta)$ is used.[1,6,7]

$$Z(\zeta) = N_n/D_n + i\sigma\pi^{1/2} \exp(-\zeta^2)$$

$$N_n = b_n N_{n-1} + a_n N_{n-2}$$

$$D_n = b_n D_{n-1} + a_n D_{n-2}$$

$$N_{-1} = 1, N_O = 0$$

$$D_{-1} = 0, D_O = 1$$

$$a_{n+1} = -n(n-1/2), \qquad n = 1, 2, 3, \ldots$$

$$b_{n+1} = -\zeta^2 + 1/2 + 2n, \qquad n = 0, 1, 2, \ldots$$

$$a_1 = \zeta$$

$$\sigma = \begin{cases} 0, & y > 0 \\ 2, & y < 0 \end{cases}$$

Region III. $|x| \geqslant 5$, $|xy| < 1.5$

First the value of $Z(x)$ is calculated from the asymptotic expansion[1] and then the value for finite y is found by another asymptotic series of Hermite polynomials in y.

$$Z(\zeta) = \exp(y^2 - 2ixy) \left\{ Z(x) + \frac{1}{x} \sum_{n=0}^{N} \frac{(-1)^n}{(2x)^{2n}} H_{2n}(0) \right\}$$

$$-\frac{1}{x} \sum_{n=0}^{N'} \frac{(-1)^n}{(2x)^{2n}} \left[H_{2n}(y) - \frac{i}{2x} H_{2n+1}(y) \right]$$

$$Z(x) = -\frac{1}{x} \sum_{n=0}^{N''} \frac{(2n-1)!!}{(2x^2)^n} + i\pi^{1/2} \exp(-x^2)$$

$$H_{k+1}(y) = 2yH_k(y) - 2kH_{k-1}(y)$$

$$H_{-1}(y) = 0, \quad H_0(y) = 1.$$

This algorithm was tested in single precision on the IBM 370 computer over the region $-10 \leqslant x \leqslant +10$, $-10 \leqslant y \leqslant +10$ at intervals of 0.1. The various summations and the continued fraction were tested for convergence by separate comparison of the relative changes in real and imaginary parts with a fixed error criterion (chosen to be 10^{-5}; much smaller values would have led to difficulty because of round-off noise in the arithmetic). Satisfactory agreement was found with the tabulated values, exclusive of the imaginary part of Z along the real axis, where the Fried and Conte[1] table is inaccurate, and no attempt was made to find more sophisticated convergence tests. The calculated values agree with the tables generally to one or two units in the fifth digit. In no case was the error more than 3 in the fifth place.

The Lamb dip laser tuning curves which were approximated in the work of Freed and Haus[4] can be calculated exactly in terms of $Z(\zeta)$. In their model a rate equation is assumed for the inversion density

$$\frac{\partial n(v)}{\partial t} = -\gamma n(v) - \int \Gamma(v', v) n(v) \, dv' + \int \Gamma(v, v') n(v') \, dv' + R(v)$$

$$- \sum_{k, \omega} \frac{2}{\hbar\omega} n(v) \sigma(v, k, \omega) |E(k, \omega)|^2 \frac{c}{8\pi},$$

where γ is a phenomenological relaxation rate, $\Gamma(v, v')$ represents the effect of velocity-changing elastic collisions, $R(v)$ is the pumping rate, $\sigma(v, k, \omega)$ is the cross section for stimulated emission into a mode of wave vector k and angular frequency ω, and $|E(k, \omega)|^2 \frac{c}{8\pi}$ is the intensity of mode (k, ω). Detailed balance requires

$$\Gamma(v', v) \, n_o(v) = \Gamma(v, v') \, n_o(v'),$$

where $n_o(v)$ is the inversion density in the presence of pumping, but with the laser field zero. It is also assumed that all velocity-changing collisions redistribute particles according to the equilibrium distribution, that is,

$$\Gamma(v', v) \, n_o(v) = \Gamma(v, v') \, n_o(v') = \frac{n_o(v) \, n_o(v')}{N_o \tau},$$

where

$$N_o = \int n_o(v) \, dv$$

and τ is another phenomonological rate. Assuming that the lasing field is small, we may take

$$\sigma(v, k, \omega) = \frac{\sigma_o}{1 + \left[\omega - \omega_o\left(1 - \frac{\overline{v} \cdot \overline{k}}{ck}\right)\right]^2 T_2^2},$$

where ω_o is the center frequency of the atomic resonance, and T_2 is the dephasing time. Carrying out the calculation outlined by Freed and Haus and assuming a uniform cavity mode, we find

$$|E_o|^2 = \frac{4\sqrt{\pi} \, \hbar \omega_o}{c\sigma_o^2 N_o y}\left(\gamma + \frac{1}{\tau}\right) \frac{G_o - L/(Z_i/\sqrt{\pi})}{1 + \frac{y^2}{|\zeta|^2} + \frac{4\sqrt{\pi} \, y}{\gamma \tau} + \left[\frac{2y}{Z_i} + \left(2x + \frac{x}{|\zeta|^2} - \frac{1}{x}\right)\frac{y Z_r}{Z_i} - 2y^2\right]},$$

where

$$x = \frac{\omega - \omega_o}{\sqrt{2} \, \Delta\omega_D}$$

$$y = \left[\sqrt{2} \, \Delta\omega_D T_2\right]^{-1}$$

$$\Delta\omega_D = (kT/m)^{1/2} \frac{\omega_o}{c}$$

$$\zeta = x + iy$$

$$Z(\zeta) = Z_r + iZ_i$$

$$G_O = 2\sqrt{\pi}\ N_o\sigma_o y.$$

The limit of (1) as $y \to 0$ with x/y constant is identical to the expression derived by Freed and Haus

$$|E_O|^2 = \frac{4\sqrt{\pi}\ \hbar\omega_o}{c\sigma_o^2 N_o y}\left(\gamma + \frac{1}{\tau}\right)\frac{G_O - L\ e^{+x^2}}{1 + \dfrac{y^2}{|\zeta|^2}}.$$

Figure XVI-38 shows a comparison of the tuning dependence of expressions (1) and (2) for parameters typical of the CO laser of Freed and Haus.[4] Since $\Delta\omega_D T_2 \approx 10$, the
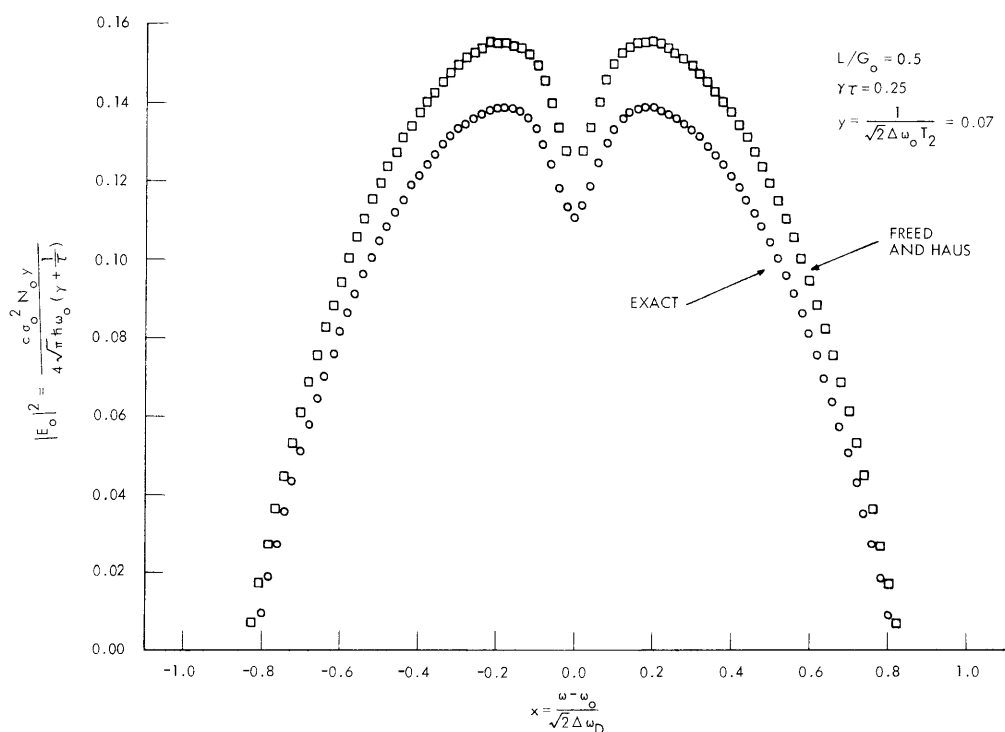

Fig. XVI-38. Comparison of exact Lamb dip expression with the Freed and Haus[4] approximation.

spectral lines are predominately Doppler-broadened, but substantial discrepancies still remain. It is clear that for accurate work, especially at higher pressures where the pressure widths will be comparable to the Doppler widths, the exact expression (1) will be necessary.

References

1. B. D. Fried and S. D. Conte, The Plasma Dispersion Function (Academic Press, Inc., New York, 1961).

2. D. H. Close, "Strong Field Saturation Effects in Laser Media," Phys. Rev. 153, 360-371 (1967).

3. A. Icsevgi and W. E. Lamb, "Propagation of Light Pulses in a Laser Amplifier," Phys. Rev. 185, 517-545 (1969).

4. C. Freed and H. A. Haus, "Lamb Dip in CO Lasers" (IEEE J. Quant. Electronics, in press).

5. P. Barberio-Corsetti, "Calculation of the Plasma Dispersion Function," Report MATT-773, Plasma Physics Laboratory, Princeton University, August 1970.

6. H. S. Wall, Analytic Theory of Continued Fractions (D. Van Nostrand Company, Inc., New York, 1948).

7. P. Henrici, "The Quotient-Difference Algorithm," in Further Contributions to the Solution of Simultaneous Linear Equations and the Determination of Eigenvalues, U.S. National Bureau of Standards Applied Mathematics Series 49, 15 January 1958.